Title

Relative Roles of Plume and Coastal Forcing on Exchange Flow Variability of a Glacial Fjord

Journal

Journal of Geophysical Research - Oceans, 129(6)

ISSN

2169-9275

Authors

Sanchez, Robert

Straneo, Fiammetta

Hughes, Kenneth

et al.

Publication Date

2024-06-01

DOI

10.1029/2023jc020492

JGR Oceans

RESEARCH ARTICLE
10.1029/2023JC020492

Special Collection:
Physical processes, sediment transport and morphodynamics of estuaries and coastal seas

Relative Roles of Plume and Coastal Forcing on Exchange Flow Variability of a Glacial Fjord

Robert Sanchez[1], Fiammetta Straneo[1], Kenneth Hughes[2], Philip Barbour[2], and Emily Shroyer[2,3]

[1]Scripps Institution of Oceanography, UC San Diego, San Diego, CA, USA, [2]College of Earth, Ocean, and Atmospheric Sciences, Oregon State University, Corvallis, OR, USA, [3]Office of Naval Research, Arlington, VA, USA

Key Points:

- We present a set of realistically forced, multi-year numerical simulations of Sermilik Fjord in Greenland
- The shelf-driven circulation is tied to along-shelf wind stress and drives a reversal in the exchange flow as winds intensify in September
- The plume-driven circulation is more effective at renewal with a flushing time 1/3 that of the shelf-driven circulation near the fjord head

Supporting Information:

Supporting Information may be found in the online version of this article.

Correspondence to:

R. Sanchez,
rmsanche@ucsd.edu

Citation:

Sanchez, R., Straneo, F., Hughes, K., Barbour, P., & Shroyer, E. (2024). Relative roles of plume and coastal forcing on exchange flow variability of a glacial fjord. *Journal of Geophysical Research: Oceans*, *129*, e2023JC020492. https://doi.org/10.1029/2023JC020492

Received 18 SEP 2023
Accepted 16 MAY 2024

Author Contributions:

Conceptualization: Fiammetta Straneo, Emily Shroyer
Data curation: Kenneth Hughes, Philip Barbour, Emily Shroyer
Formal analysis: Robert Sanchez
Funding acquisition: Fiammetta Straneo, Emily Shroyer
Methodology: Robert Sanchez, Kenneth Hughes
Supervision: Fiammetta Straneo
Validation: Robert Sanchez, Philip Barbour, Emily Shroyer
Writing – original draft: Robert Sanchez
Writing – review & editing: Robert Sanchez, Fiammetta Straneo, Kenneth Hughes

Abstract Glacial fjord circulation determines the import of oceanic heat to the Greenland Ice Sheet and the export of ice sheet meltwater to the ocean. However, limited observations and the presence of both glacial and coastal forcing—such as coastal-trapped waves—make uncovering the physical mechanisms controlling fjord-shelf exchange difficult. Here we use multi-year, high-resolution, realistically forced numerical simulations of Sermilik Fjord in southeast Greenland to evaluate the exchange flow. We compare models, with and without a plume, to differentiate between the exchange flow driven by shelf variability and that driven by subglacial discharge. We use the Total Exchange Flow framework to quantify the exchange volume transports. We find that a decline in offshore wind stress from January through July drives a seasonal reversal in the exchange flow increasing the presence of warm Atlantic Water at depth. We also find that including glacial plumes doubles the exchange flow in the summer. Our results show that the plume-driven circulation is more effective at renewal with a flushing time 1/3 that of the shelf-driven circulation near the fjord head.

Plain Language Summary Glacial fjords are narrow coastal inlets with a glacier at the landward edge. The flow of water within fjords plays a crucial role in exchanging heat and freshwater between the glacial ice and ocean. The circulation of water is driven, in part, by melting at the ice surface which falls through cracks in the ice and enters the fjord near the sea bed. The meltwater is less dense than ocean water causing it to rise as a plume before leaving the fjord close to the surface. However, fjord circulation is also impacted by storms close to the coast and offshore wind. We used a model of a fjord in Greenland to isolate and study the effects of coastal winds and meltwater on fjord circulation. Our model experiments reveal that weaker than average winds can lead to warmer water within the fjord. Also, we find that the circulation speed doubles with the addition of meltwater and a plume. These results increase our understanding of fjord circulation.

1. Introduction

Glacial fjords are narrow coastal inlets that connect the Greenland Ice Sheet (GrIS) with the continental shelf. Fjord dynamics are responsible for the import of oceanic heat to the GrIS and the export of ice sheet meltwater to the ocean. The fjord exchange of heat and salt at the fjord mouth, along with vertical mixing within the fjord, modifies water properties including ocean heat content and stratification. These properties ultimately set the boundary conditions for ice-ocean interactions (Hager et al., 2022; Holland et al., 2008; Mortensen et al., 2018; Shroyer et al., 2017; Straneo & Cenedese, 2015; Straneo et al., 2011; Wood et al., 2021). Understanding fjord-shelf exchange is therefore crucial to predicting the impact of the ocean on marine-terminating glaciers and the consequences of exported freshwater on regional circulation and ecosystems (Hopwood et al., 2020; Rysgaard et al., 2003; Straneo & Heimbach, 2013).

Numerous drivers influence glacial fjord exchange on hourly to seasonal timescales. At the fjord mouth, circulation can be influenced by tides (Mortensen et al., 2011), external water mass variability (Schaffer et al., 2020), continental shelf wind variability (Jackson et al., 2014) and coastal-trapped waves (Gelderloos et al., 2021). Within the fjord, circulation is modified by mixing (Hager et al., 2022), internal waves (Inall et al., 2015), surface heat fluxes (Mortensen et al., 2011), local winds (Moffat, 2014), and iceberg melt (Davison et al., 2020). At the glacial boundary, or fjord head, additional forcing comes from surface runoff (Stuart-Lee et al., 2021), subglacial discharge (Carroll et al., 2015; Slater & Straneo, 2022), and submarine melting of the terminus (Zhao, Stewart, & McWilliams, 2022; Slater et al., 2018). Untangling the individual role of these drivers is challenging because many of the effects are cumulative and difficult to isolate with limited observations (Straneo et al., 2019). In this study, we will focus on the relative roles of plume forcing and shelf forcing (e.g., winds, coastal-trapped waves)

on fjord circulation, as these are the two dominant forcing mechanisms of fjords in southeast Greenland (Fraser & Inall, 2018; Gelderloos et al., 2022; Jackson et al., 2014; Jackson & Straneo, 2016).

Glacial fjords undergo substantial seasonal variability in both shelf and glacial forcing that complicates diagnosing drivers of fjord circulation (Hager et al., 2022; Jackson & Straneo, 2016; Mortensen et al., 2014). Glacial forcing from submarine melting and ice sheet meltwater runoff is strongest in summer, but shelf-forcing seasonality is dependent on factors such as sea ice, boundary currents and wind forcing which can vary regionally (Carroll et al., 2018; Gelderloos et al., 2017; Gladish, Holland, & Lee, 2014). Observations are biased toward the summer and away from ice-congested areas, limiting comparisons between glacial-driven circulation and shelf-driven circulation. Consequently, we lack a deep understanding of the relative role of the shelf-driven circulation versus plume-driven circulation in setting fjord properties seasonally and how these circulation modes vary along fjord.

Models of glacial fjords have been a useful tool in isolating different forcing mechanisms and overcoming data limitations. Very high-resolution (<10 m) models have brought insight into the dynamics of subglacial discharge plumes (e.g., Carroll et al., 2015; Ezhova et al., 2017; Kimura et al., 2014; Sciascia et al., 2013; Xu et al., 2012) and led to plume representation into larger fjord models (T. Cowton et al., 2015; Jenkins, 2011; Rignot et al., 2016). Fjord-scale models have allowed for an assessment of the impact of along-fjord winds, along-shelf winds and shelf forcing on fjord dynamics (Fraser & Inall, 2018; Jackson et al., 2018; Sundfjord et al., 2017), of iceberg melt on water mass transformation (Davison et al., 2020; Kajanto et al., 2023), of sea ice retreat on fjord circulation (Shroyer et al., 2017), and of fjord geometry, including ice mélange, on fjord renewal (Gladish, Holland, Rosing-Asvid, et al., 2014; Carroll et al., 2017; Zhao et al., 2021; K. G. Hughes, 2022). While these models have significantly improved our understanding of glacial fjord processes, they are usually run on idealized bathymetry or with idealized forcing limiting any comparison with observations. More realistic models without these idealizations and that are evaluated against observations are needed. These models can help identify the time-integrated response of fjords to seasonally-varying forcing and to generate the complex circulation patterns seen in observations.

We use a high-resolution, realistic model of Sermilik Fjord, in southeast Greenland, forced by a wind-reanalysis product and boundary conditions from a larger pan-Arctic state estimate, to differentiate between the shelf-driven and subglacial-discharge-driven exchange flow. Comparison with observations shows that the model reproduces the relevant dynamics over multiple years and through seasonal transitions. We split the results into two sections with one focused on describing model circulation and properties (Section 4), and the other analyzing the exchange flow (Section 5). We find the seasonality of the along-shelf winds drives reversals in the circulation, the exchange flow is primarily plume-driven during the summer, and the plume-driven circulation is more effective at renewal than the shelf-driven circulation. Understanding the response of fjord-shelf exchange to simultaneous external and internal forcing is a critical step toward improved representation of ice-ocean interactions in climate models.

2. Background on Sermilik Fjord System

Sermilik Fjord (SF) is part of a large glacial fjord system in southeast Greenland (Figure 1, inset map). The fjord varies in width from 5–10 km, is 550–900 m deep, and is about 80 km long before branching into three fjords connecting to Helheim, Fenris and Midgaard glacier from west to east (Figure 1). Midgaard Glacier has experienced the greatest cumulative loss of the three glaciers over the past 40 years (138 ± 5 Gt, Mouginot et al., 2019). However, Helheim Glacier is currently one of the largest outlet glaciers in Greenland (35 Gt/yr, Mankoff et al., 2020; Enderlin et al., 2014) and saw a rapid acceleration and thinning in the 2000s (Howat et al., 2005; Luckman et al., 2006). Increased submarine melting due to relatively warm water at depth and circulation enhanced by ice sheet runoff has been proposed as a likely trigger for retreat (Holland et al., 2008; Jackson et al., 2022; Khazendar et al., 2019; Slater & Straneo, 2022; Straneo et al., 2011; Wood et al., 2018, 2021).

The water masses present in the fjord determine the heat available for melting. SF has a deep sill (500 m) that is far from the mouth allowing significant water column exchange with the shelf (Jackson et al., 2014; Straneo et al., 2010). As a result, the water masses in the fjord broadly match those found on the adjacent shelf and are steered into SF through Sermilik Trough, a deep trough that cuts across the eastern part of shelf before running parallel to the coastline (Figure 1; Harden et al., 2014; Straneo et al., 2011; Snow et al., 2021). During the winter, SF is dominated by two water masses: cold and fresh Polar Water (PW) of Arctic origin and a deep, relatively

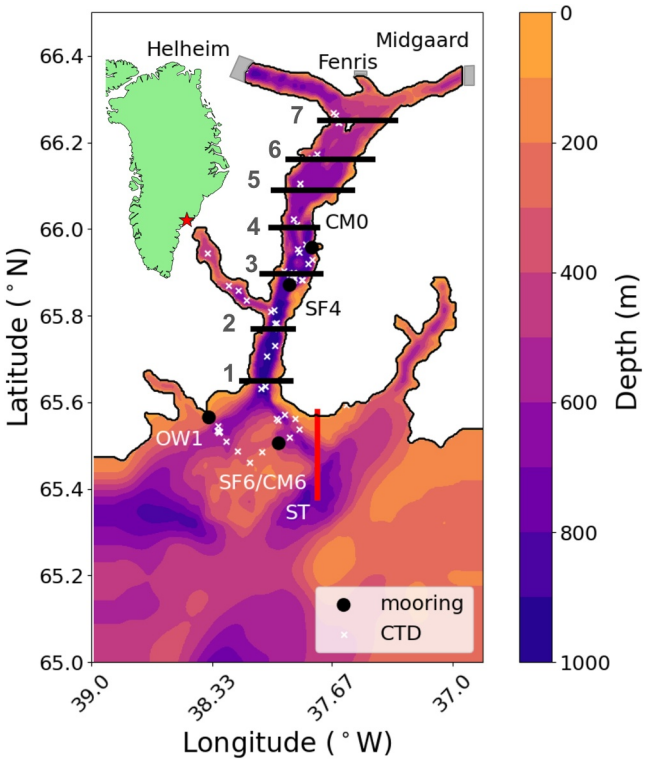

Figure 1. Model domain and bathymetry. In black are the gates used for the calculation of Total Exchange Flow (TEF) transports in Sermilik Fjord. The red line is the coastal section used for the shelf seasonality analysis. The locations of observations used in the model comparison are given in black circles (moorings) and white crosses (CTD). The glacier names are given at the top. Sermilik Trough (ST) is shown in white text. The inset map shows the location of Sermilik Fjord in the context of Greenland.

warm and salty water of Atlantic origin (AW) (Sup. Figure 1). During the summer, a third water mass, Warm Polar Water (WPW), is formed on the shelf from surface warming of PW and intrudes into fjords (Sutherland et al., 2014). Mixing across the shelf and trough determine the relative volumes of these water masses within the fjord (Harden et al., 2014; Snow et al., 2021).

In addition to shelf water masses, two types of meltwater are released into the fjord and affect fjord circulation and water properties. Submarine meltwater forms locally when icebergs and glaciers melt in the ocean, and subglacial discharge forms through surface melting of the ice sheet and enters the fjord at depth. Subglacial discharge generates a turbulent buoyant plume which drives an overturning circulation, upwells warm and salty AW into shallower depths and enhances submarine melting (Beaird et al., 2018; Carroll et al., 2015; Jackson et al., 2022; Slater et al., 2022; Slater & Straneo, 2022). The upwelled AW is many times the volume of the original subglacial discharge flux and can displace PW that was previously near the head of the fjord (Beaird et al., 2018; Mankoff et al., 2016). Therefore, both glacial and shelf processes influence the amount of AW (and heat) within the fjord.

Observations have shown that the circulation in SF is strongly influenced by shelf forcing (Jackson et al., 2014; Snow et al., 2021; Straneo et al., 2010). Shelf winds primarily flow southwestward and parallel to the coast resulting in downwelling conditions that generate large pycnocline displacements. These displacements create a density gradient within the fjord initiating baroclinic circulation with shallow inflow and deep outflow (Aure et al., 1996; Jackson et al., 2014; Klinck et al., 1981). As the pycnocline relaxes, the circulation reverses. Many of these events are correlated with observable pulses within Sermilik Fjord and are associated with 3–7 day periods, 40 cm/s speed and large heat and salt transports (Jackson et al., 2014; Straneo et al., 2010). The fjord heat content is dominated by pycnocline fluctuations which change the relative volumes of AW and PW and can obscure the influence of glacial forcing (Jackson & Straneo, 2016; Sanchez et al., 2021). These fluctuations have been linked with coastal-trapped waves, a term used to describe a range of both barotropic and baroclinic wave phenomena in which trapping by rotation leads to propagation along continental shelves and coasts (Fraser & Inall, 2018; Jackson et al., 2018). In Greenland, where bathymetry is steep, these waves behave like internal Kelvin waves and propagate along the shelf and fjord with the shore to the right (Jackson et al., 2018).

As described above, subglacial discharge can initiate plumes at the heads of glacial fjords. Plumes drive an overturning circulation which enhances background melting (Slater et al., 2018; Jackson et al., 2020; Zhao, Stewart, & McWilliams, 2022; Zhao, Stewart, McWilliams, Fenty, & Rignot, 2022). The outflowing plume volume transport is primarily composed of ambient water entrained within the plume as it rises (Mankoff et al., 2016), and the plume is a significant source of water mass transformation. The outflowing plumes can interact with nearby bathymetry and drive recirculation in the fjord (Slater et al., 2018; Zhao, Stewart, & McWilliams, 2022). Thus, the influence of the plume-driven circulation on fjord-shelf exchange is a function of both subglacial discharge and fjord geometry.

Previous simulations of Sermilik Fjord (or idealized versions) have focused on coastal-trapped waves (Gelderloos et al., 2022; Jackson et al., 2018), subglacial discharge plumes (Sciascia et al., 2013), the impact of icebergs (Davison et al., 2020) and standing eddies, which spin up over month time scales and occur in models with realistic geometry but steady (time-invariant) forcing (Zhao, Stewart, McWilliams, Fenty, & Rignot, 2022). However none of these studies involved the use of a full 3-dimensional model with realistic bathymetry and time-varying realistic forcing. Most of the previous models were run to steady-state and examined the fjord response to the input of glacial meltwater. Therefore, they could not capture seasonal transitions and the time-integrated response of fjord properties to external forcing.

3. Model Setup and Forcing

We ran nearly 3-year simulations (2015–2017) of a regional model of Sermilik Fjord and its adjacent shelf (Figure 1) using the hydrostatic-configuration of the MITgcm (Adcroft et al., 2004; Marshall et al., 1997). The model domain is 360 by 640 cells with an isotropic horizontal resolution of 280 m by 280 m. The model was configured with 32 vertical levels varying from 10-m resolution in the upper 200 to 100-m resolution at 950 m depth. Model bathymetry is based on BedMachine v3 (Morlighem et al., 2017). The maximum depth within SF was 920 m (Figure 1). Advection of temperature and salinity uses a third-order flux limiter scheme. The standard time step for the model was 60 s but reduced occasionally for model stability. Output snapshots, including temperature, salinity, velocity and sea surface height are saved every 3 hr.

The model was configured with a nonlinear equation of state following Jackett and Mcdougall (1995). Mixing is parameterized using the KPP vertical mixing scheme (Large et al., 1994) with a background viscosity of 10^{-4} m^2 s^{-1} and diffusivity for temperature and salinity of 10^{-5} m^2 s^{-1} in the vertical. In the horizontal, the set-up used a non-dimensional harmonic viscosity of 0.01, which equates to approximately 3 m^2 s^{-1} for the isotropic configuration, modified by a non-dimensional Smagorinsky scheme with coefficient 3 following Griffies and Hallberg (2000). A quadratic drag coefficient of 2×10^{-3} was applied at the bottom.

Simulation initialization and boundary forcing is taken from the Arctic Subpolar Gyre State Estimate "ASTE" (Nguyen et al., 2021). Initial temperature, salinity and velocity fields were generated from a spin-up simulation of 3 months in which the boundary forcing was held steady and no surface forcing was applied. On each of the three boundaries on the shelf, there are sponge regions that are 20 grid cells wide in which T, S, U, and V are relaxed to the ASTE values with time scales of 3 hr on the outer edges and 30 hr on the inner edges. Boundary fields are updated daily and linearly interpolated onto each model time step. A constant offset in temperature (−1.5°C) and salinity (−0.3) was applied to the ASTE fields to tune to available mooring and profile records near the mouth of Sermilik Fjord (Figure 2).

Model surface forcing was taken from ERA5 (Hersbach et al., 2020). Surface fluxes were generated within MITgcm external forcing module using 10-m winds, humidity, air temperature, and downward shortwave and longwave radiative fields. Surface forcing fields were updated hourly with a linear interpolation to simulation time steps. While ERA5 realistically simulates shelf forcing, the fjord is largely unresolved. Tides are neglected from this model, as the synoptic variability (1–10 days) dominates over tidal variability (Jackson & Straneo, 2016; Sutherland et al., 2014).

It should be noted that sea ice is neglected in these model runs. Sea ice generally reaches Sermilik Fjord starting in December and can persist until as late as July (NASA Worldview). Sea ice can impact the momentum transfer of wind and can cause a deflection in the angle of Ekman transport (Rabinovich et al., 2007). However, both of these effects should only change the magnitude of circulation response to wind stress and not the qualitative features of the circulation within the fjord. A sea ice cover was included in the Fraser and Inall (2018) and Fraser et al. (2018) studies of coastal-trapped waves in southeast Greenland. We observe similar coastal-trapped wave phenomena to them giving confidence that the fjord response to coastal wind stress is robust. However, we acknowledge some uncertainty in the magnitude of the fjord response to coastal wind stress.

For a brief description of the wind forcing, we plot the wind stress on the shelf at the southern edge of the coastal transect (Location in Figure 1).The along-shelf wind stress (oriented such that northeasterly wind is negative) is almost always downwelling favorable (Figure 3). Individual wind events can be intense reaching magnitudes as high as 0.8 N/m^2. A low-pass wind stress representative of seasonal wind patterns, τ_{lp} is calculated using a 90 days, 6th order Butterworth filter. τ_{lp} shows the winds are strongest from November to May and weakest from June to August (Figure 3a).

We compare two 3-year simulations in this manuscript. The first is configured as described above without representation of the glacial runoff and melt. This run is referred to as the "No Glacier" (NG) run. The second is referred to as the "With Glacier" (WG) run. Within the WG run, subglacial discharge plumes and glaciers were added to the three glaciers at the north end of SF (those named in Figure 1). This cold, fresh water originates as surface melt of the glacier, and peaks in summer. It makes its way through to the base of the ice sheet and enters the ocean at depth at the grounding line to become a buoyant, turbulent plume. Within the WG run, plume dynamics are parameterized following T. Cowton et al. (2015). We use the half-cone plume configuration, and each glacier has one plume confined to a single horizontal grid cell. Discharge values come from regional climate

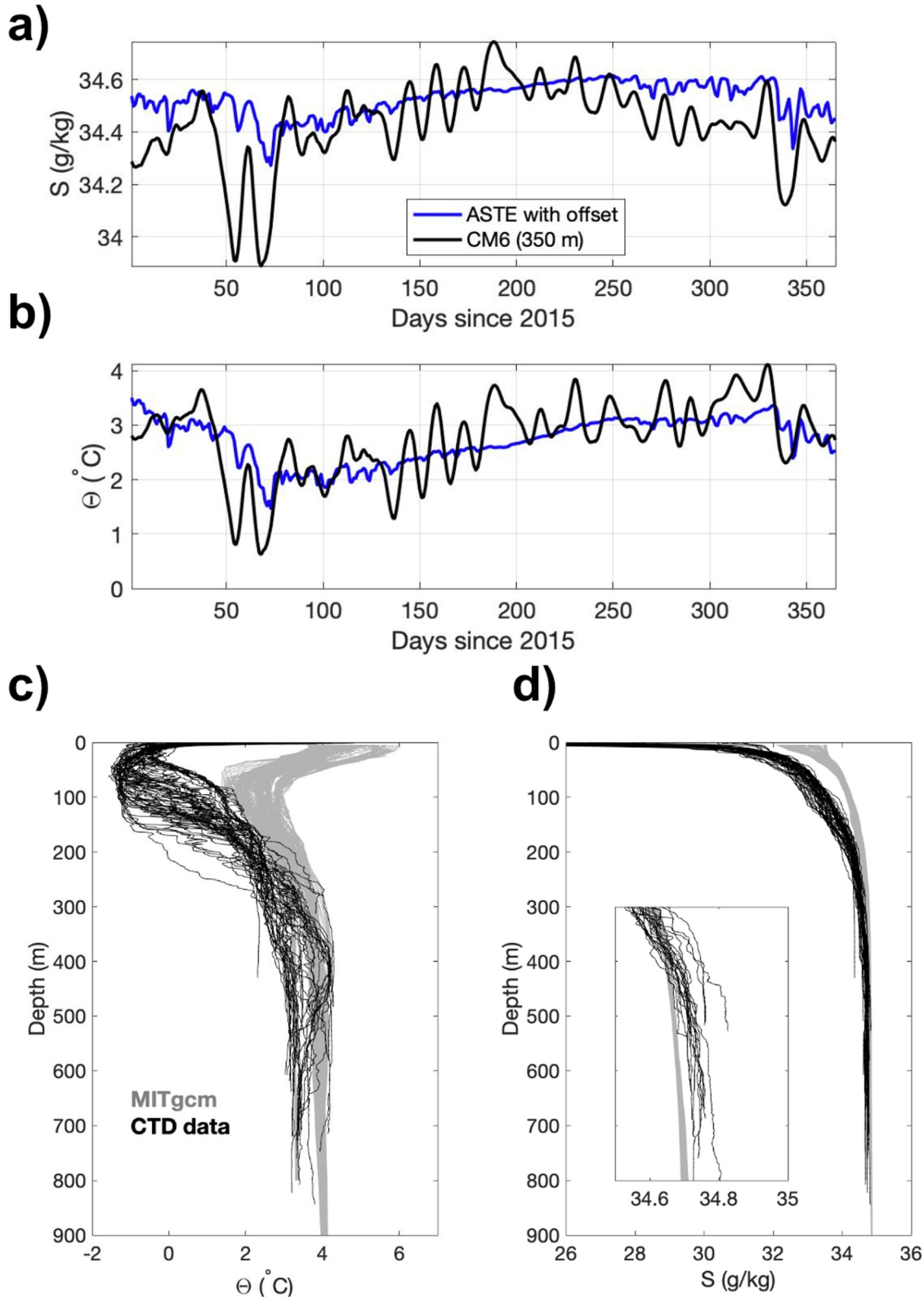

Figure 2. (a, b) Comparison of ASTE boundary conditions with shelf mooring located at CM6 (Figure 1). (c, d) comparison of model output from Sermilik Fjord over the months of July 2017 and August 2015 against CTD profiles taken in July 2017 and August 2015. The inset in panel d is a zoom on the region between 34 and 36 g/kg. The *y*-axis is shared with the larger figure.

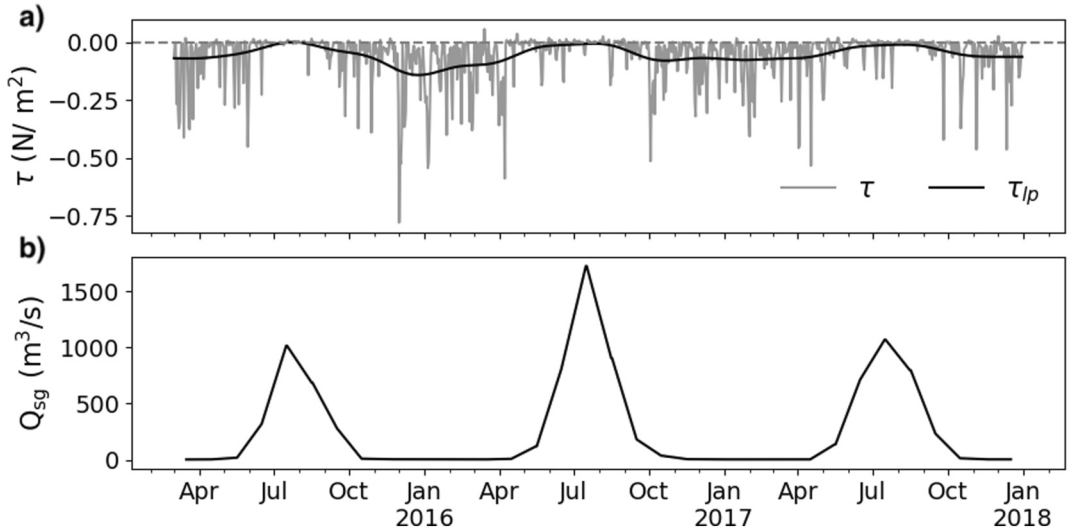

Figure 3. (a) Along-shelf wind stress peaks in winter. The daily along-shelf wind stress is in gray and the 90-day low-pass wind stress (τ_{lp}) is in black. Negative is toward the southwest. (b) The total subglacial discharge (Q_{sg}) flux in the With Glacier (WG) run.

simulations compiled by Slater et al. (2020). A constant discharge is used for each month. Subglacial discharge is applied to all months and varies interannually (Figure 3). Peak discharge in the summer at each glacier is 300–600 $m^3\ s^{-1}$. Discharge in the winter is 2–5 $m^3\ s^{-1}$. This run also includes melt cells across each glacier iceface, but the input from directly melting the vertical glacier at the ice-ocean interface is negligible. Therefore, the main difference between NG and WG are the effects of the subglacial discharge plume and we will refer to circulation initiated by glacial forcing as the "plume-driven" circulation. The NG and WG simulations were identical apart from the addition of glacial plumes.

A full comparison of the model output against observational data is given in Appendix A, but is briefly described here. Both visually (Figure 2; Figure A1) and quantitatively, the model does a reasonable job of recreating the temperature and salinity variability seen in the observations. The mooring data on the shelf is significantly correlated in salinity ($r = 0.75$) and temperature ($r = 0.51$) over 30-day timescales. Additionally, both the salinity and temperature were significantly correlated on higher-frequency timescales (<30 days) giving confidence that higher shelf-forcing is reasonably represented (Table A1). The volume transport in the model does not deviate substantially from the estimates of the transport from the observations, although it does underestimate the summer transport (Figure S2 in Supporting Information S1). However, the observed volume transport itself might be biased as it is calculated from a single mooring and assumes no horizontal shear.

We find that the model cannot reproduce the shallower properties such as PW salinity and stratification (Figure 2). We attribute the model bias to missing freshwater sources such as icebergs, sea ice and surface runoff, and to poor representation of surface forcing within the fjord. Other models (Davison et al., 2020; Kajanto et al., 2023) and observations (Moon et al., 2018) suggest the freshwater transport from icebergs can increase the strength of circulation and significantly modify (cool and freshen) shallow fjord properties increasing stratification. Recently, Kajanto et al. (2023) showed, for a similar large fjord in west Greenland, that without icebergs the model could not reproduce the observed properties. There is also some bias likely introduced from the ASTE boundary conditions which underestimates freshwater in the East Greenland Current (Nguyen et al., 2021). In this model iteration, the atmospheric surface forcing is too coarse to be well resolved within the fjord and misses occasional but strong downfjord wind events. More research is needed to determine which of these biases is responsible for the shallow properties mismatch between model and observations.

Despite these biases, we believe the model dynamics are representative of dynamics in the real Sermilik Fjord. As discussed above, the lack of sea ice might change the magnitude of fjord response to wind stress, but should not change the qualitative picture. The model does not have accurate stratification and so our plume reaches the surface rather than outflowing at around 100 m depth (Figure S1 in Supporting Information S1). However, we

have confidence that plume theory represents plume dynamics appropriately (Mankoff et al., 2016) and that the overturning generated by the plume parameterization is realistic (T. Cowton et al., 2015). While the stratification impacts the depths of currents in the model, the baroclinic response to downwelling winds shows inflow above the pycnocline, consistent with observations (Jackson et al., 2014). Consequently, our results are focused on shelf-forcing and plume transport, both of which appear reasonably well represented.

4. Analysis of Circulation and Properties

4.1. Shelf Circulation and Variability

On its ocean boundary, SF is externally forced by the circulation and variability on the continental shelf. The shelf outside SF is characterized by the confluence of PW carried in from the coastal current (East Greenland Coastal Current, EGCC) and AW transported along Sermilik Trough (ST, Figure 4). Closer to the surface, the EGCC can be seen as a westward flowing current carrying relatively cold water (Figure 4a). The gradient between these two water masses is relatively diffuse indicating lateral mixing over the shelf and trough. At greater depths, relatively warm AW is steered into the fjord along ST, although there are recirculation cells within the trough system (Figure 4b). The across-shelf isopycnal gradient (discussed later this section) sinks toward the coast resulting in lighter, cooler water closer to the fjord at a fixed depth (Figure 5).

The shelf properties upstream (east) of SF (Figure 1, red line) vary in response to both wind forcing and external water mass variability. Two month averages of temperature in the NG run are highest in the fall (September–October) and coolest in the spring (March–April, Figure 5). In September, when the waters on the shelf are warmest, the AW extends all through the water column and onto the shelf (Figure 5e). During the rest of the year, a cold PW cap is present close to the coast, however its lateral extent appears variable and dependent on the steepness of the isopycnal slope. The density gradients across the shelf are strongly correlated with the daily along-shelf wind stress ($r = 0.78$). Therefore, the isopycnals are compact and relatively flat in the summer months when the winds are weaker. The isopycnals start to steepen in the fall and early winter in response to downwelling-favorable winds. When the isopycnals are steepest, the volume ratio of cold PW to warm AW is highest. Additionally, the coastal current is strongest in the fall and winter when isopycnals are steepest (Figure 6), consistent with geostrophy. The upstream transect shows little difference in properties between the NG and WG run (not shown), and therefore, we assume the forcing associated with isopycnal displacement on the shelf is active and equivalent in both runs.

We also examined the coastal current downstream (west) of the fjord. The NG and WG runs diverge and a relatively fresh wedge can be observed close to the coast in the WG run July through September (Figure S3 in Supporting Information S1). However, in these downstream sections we do not observe substantial differences in temperature or current velocity (Figures S3 and S4 in Supporting Information S1).

4.2. Fjord Circulation and Properties (No Glacier)

In the NG run, the circulation in the fjord responds to shelf forcing driven in large part by local, along-shelf winds. To examine the circulation, we focus on a cross-section at SF Line 3 as this location is closest to the mooring SF4 and is representative of circulation away from mixing processes at the head and the mouth of the fjord. We find that the circulation at the SF Line 3 varies seasonally, exhibits signs of being rotationally-influenced and is characterized by reversals with depth (Figures 7a–7c). The strongest average flow is observed in spring with inflow at depth and outflow around 100 m. By October, the circulation at depth has reversed. The time-varying aspects of this circulation will be examined in greater detail in Section 5.

Compared to the shelf section, variability of temperature and density along fjord is weak (Figures 8a–8c). Isopycnals lie flat within the fjord and only have a notable slope in the upper 100 m and approaching topography. The fjord shoals from 900 m at the mouth to 500 m near the branching point (70 km) and increases in depth again as it approaches Helheim glacier (90 km). The 27.45 kg/m^3 isopycnal associated with deep, relatively warm water can be seen to reach its shallowest depth (and maximum thickness) of 250 m during July, and is at its deepest at 500 m during October. However, the layers above it warm substantially in the fall and so the fjord is at its warmest in October.

A width-averaged overturning streamfunction demonstrates the changes in fjord circulation between April and October 2017. The overturning circulation is positive in April with inflow at depth and outflow near the surface

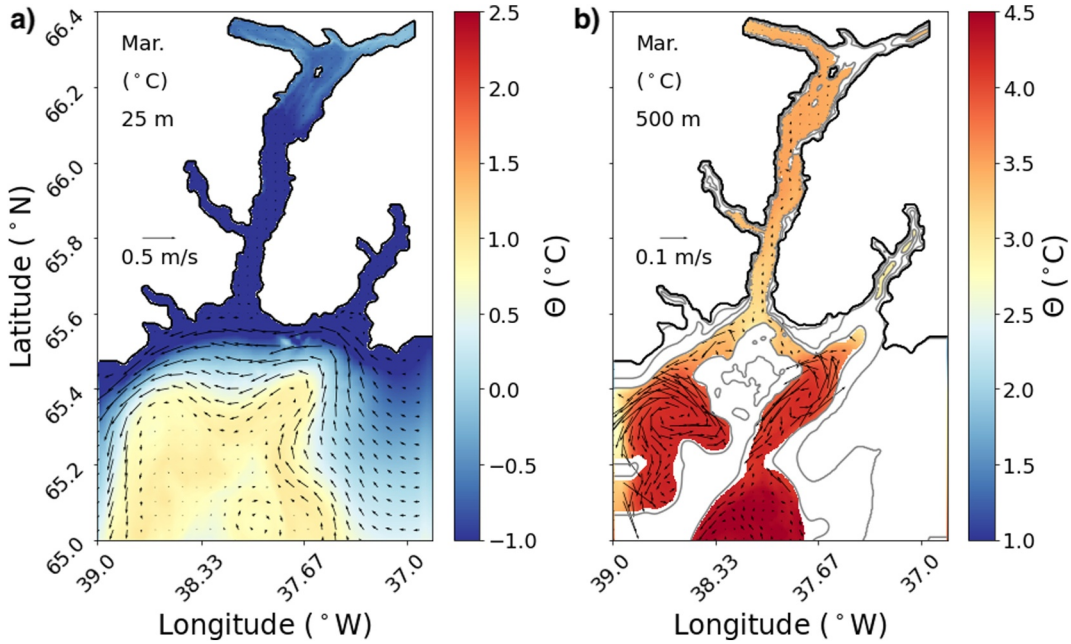

Figure 4. Plan view of temperature (color) and velocity (vectors) showing the coastal current at 25 m and the inflowing Atlantic Water (AW) at 500 m in Sermilik Trough. Each figure is produced from the monthly average (March 2017) of temperature and velocity from the No Glacier (NG) run at (a) 25 m depth and (b) 500 m depth. The depth contours are 100, 250 and 450 m. Note the different colorbars and velocity scales between the two panels.

(Figure 9a). In July, the circulation is reduced (Figure 9b). By October, the circulation appears fully reversed (Figure 9c). We should note that in 2017, the streamfunction was only reversed at depth and a three-layer system was present (not shown).

In the absence of glacial forcing (NG run), the mid-fjord properties (red, Figure 10) mirror the shelf variability (black, Figure 10) in temperature and salinity (TS) space. WPW is found seasonally near the surface ($\Theta \approx 8$°C), PW ($\sigma \approx 27.0$ kg/m^3) is found at the temperature minimum, and AW is the saltiest and densest water ($\sigma \approx 27.5$ kg/m^3). We see that in the winter months (January–April) the fjord model properties lie in between PW and AW, and the fjord can be described as a two-layer system (Figure 10, Sanchez et al., 2021). As the surface warms, a distinctive "U" shape forms from the three water masses present: WPW, PW and AW. As the surface cools, the system starts adjusting back toward a two-layer system.

To summarize the results of this section: across-shelf isopycnal gradients are steepest in winter when the winds are strongest, fjord circulation is influenced by rotation but still exhibits vertical shear, and streamfunctions demonstrate significant seasonal variability including reversals in mean fjord circulation.

4.3. Fjord Circulation and Properties (With Glacier)

The other model run includes glacial forcing (WG) with the glacial forcing dominated by the subglacial discharge plume. The inclusion of subglacial discharge plumes alters the fjord circulation and temperature, especially in summer. At SF Line 3, there is substantial difference between the WG and NG runs in July, with a much stronger outflow near the surface and less recirculation in the middle part of the fjord in the WG run (Figures 7d–7i). The non-summer months (April and October) show a weaker difference in velocity magnitude and structure between the two model runs. Taken as a whole, the fjord cross-sections demonstrate that the spatial structure of the circulation is complex and highly variable. In this study, we are primarily interested in overturning (vertical shear) and therefore will be analyzing width-integrated exchange flows.

The July temperature distribution in the fjord is similar in WG and NG except in upper 100 m where it is 2°C warmer than in the NG run (Figure 8d). This difference can be attributed to subglacial discharge entraining ambient AW and bringing it up to shallower depths via the plume. The overturning streamfunction in the WG run shows the plume drives strong outflow near the surface (Figure 9d).

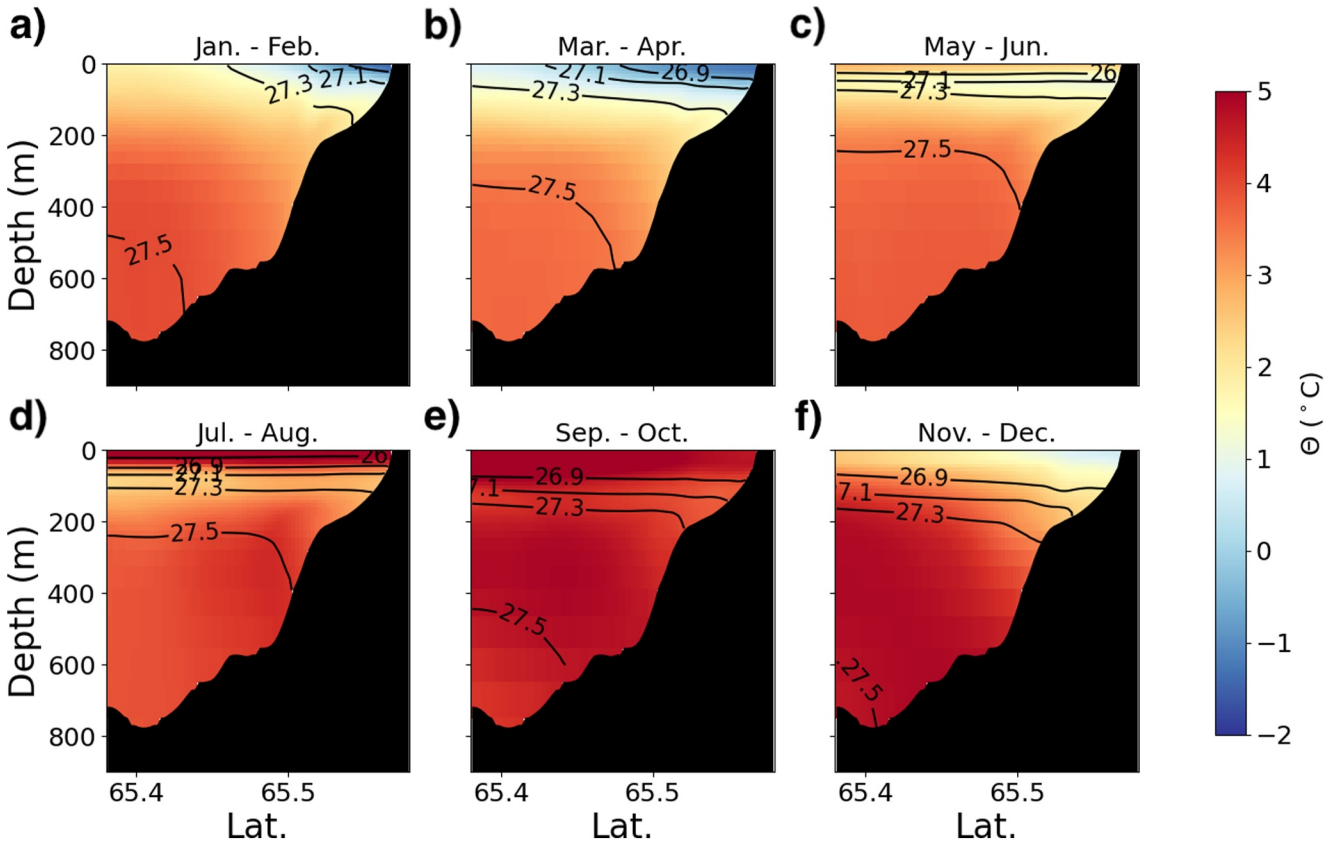

Figure 5. Isopycnals separating surface and trough waters are flat in the summer months and steep in the winter months. Each panel shows 2 month averages of coastal section temperature (No Glacier run, see Figure 1 for location). View is facing west and is perpendicular to coastal current. Contours are isopycnals of potential density anomaly (26.5, 26.9, 27.1, 27.3, 27.5).

The T-S properties in the WG run reveal the influence of the plume on fjord water properties. To aid in interpretation, we include a subglacial-discharge-mixing line (gray dashed, Figure 10) that connects AW properties with subglacial discharge properties (0°C, 0 g/kg). The WG run (blue, Figure 10) starts diverging substantially from the NG run in June due to large amounts of subglacial discharge. This divergence follows the subglacial-discharge-mixing line, and the end result is a cooler and fresher surface water mass and the "erasing" of the clear PW signal (temperature minimum). The WG run properties converge back to those of the NG run in October, and therefore we can state that the time period of subglacial discharge influence is June–September. We tested for freshwater storage by calculating the lag between subglacial discharge input and peak freshwater export (Sanchez et al., 2023). We did not observe significant freshwater storage. The peak export averaged a 2-week delay over the 3 years which we attribute to the transit time of water (0.1 m/s) across the fjord.

The summer and winter CTD observations are included in the T-S plots for context. A melt-mixing line (gray solid, Figure 10) was added which indicates how ocean properties would be modified if they were involved in melting. It connects AW properties with a melting endmember (−90°C, 0 g/kg) that takes into account the latent heat loss associated with melting (Gade, 1979). The CTD observations show that the model surface waters are biased warm during the summer, likely due to a lack of sufficient melting.

5. Exchange Flow Analysis

5.1. Introduction to the Exchange Flow

The transport of heat, salt, nutrients and other tracers out of the fjord is set by the exchange flow. In traditional estuaries, the exchange flow describes the subtidal mean circulation, typically with inflowing salty water at depth and outflowing fresher water near the surface (MacCready & Geyer, 2010). A key characteristic of the classic exchange flow is that the circulation, set up by river input and mixing, drives a volume transport out of the estuary

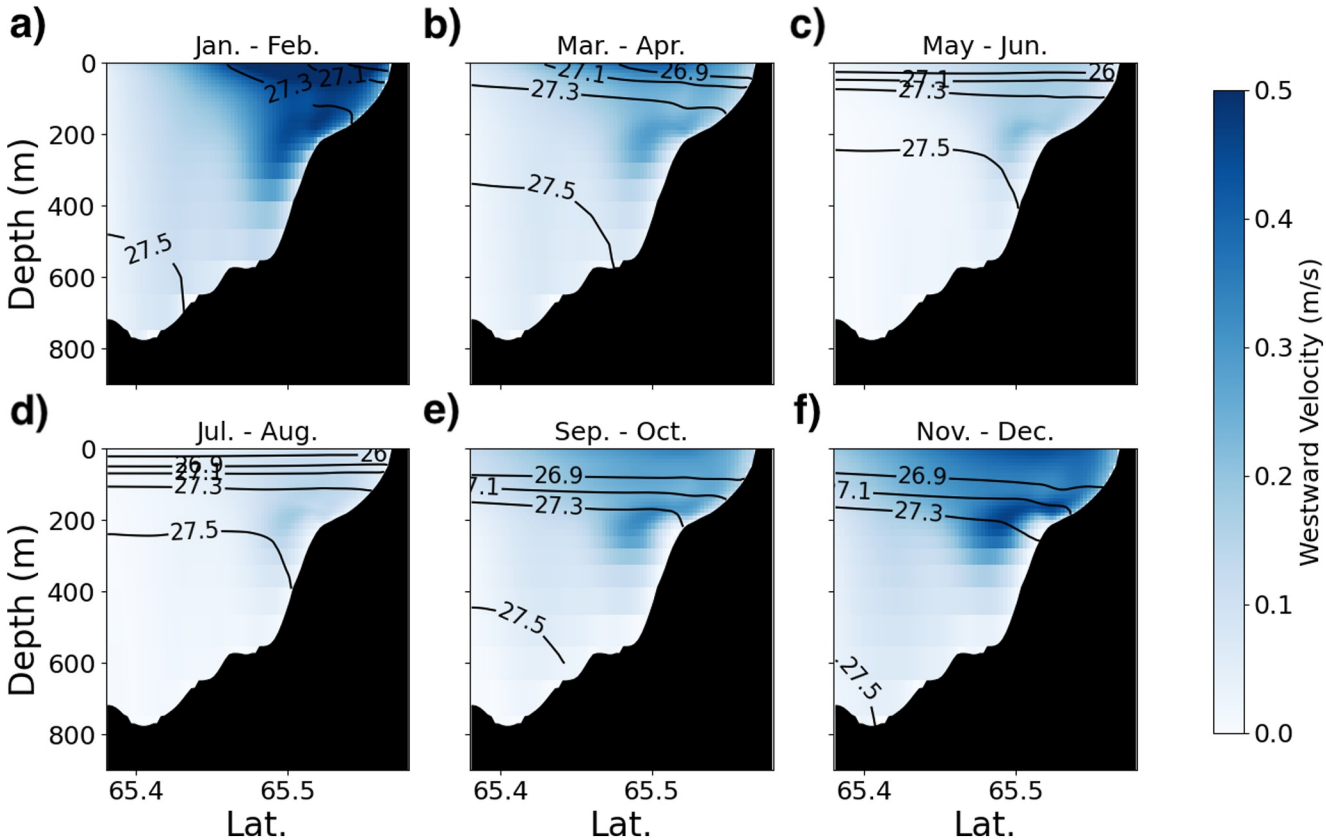

Figure 6. The coastal current is strongest in winter and weaker in summer. Each panel shows 2 month averages of westward velocity ($-U$) (No Glacier runs). View is facing west and is perpendicular to coastal current. Contours are isopycnals of potential density anomaly (26.5, 26.9, 27.1, 27.3, 27.5).

many times greater than the initial freshwater volume discharge. Applying the exchange flow concept to deep glacial fjords, we let wind-driven variability (1–10 days) play the role of tides (high-frequency oceanic variability) and glacial freshwater to play the role of river input (buoyancy) in setting up a low-frequency exchange flow (Jackson & Straneo, 2016). Using the exchange flow framework, we can analyze the role of shelf and glacial forcing in setting fjord properties.

We would like to analyze the exchange flow in terms of area-integrated, temporally-averaged or bulk properties. These properties include incoming/outgoing volume transport Q_{in}, Q_{out}, a transport-weighted incoming/outgoing Salinity S_{in}, S_{out}, a transport-weighted incoming/outgoing Temperature Θ_{in}, Θ_{out} and a transport-weighted incoming/outgoing Potential Density anomaly σ_{in} and σ_{out}. If the bulk properties are calculated directly from the model in depth coordinates, then the contributions to the salt flux from temporal correlations (e.g., $\langle u's' \rangle$, where $'$ denotes deviation from the mean) need to be accounted for. The Total Exchange Flow (TEF) method (Burchard et al., 2018; Lorenz et al., 2019; MacCready, 2011; MacCready et al., 2018) calculates the bulk properties in salinity coordinates and includes contributions from temporal correlations. While TEF averages are typically calculated in salinity coordinates, we use density coordinates to calculate volume exchange (Lorenz et al., 2020). We use density coordinates because the overall pressure gradient is effected by both temperature and salinity variability. While density coordinates are used for volume transport, when considering salt or heat budgets, salinity and temperature coordinates are necessary (Lorenz et al., 2020). Therefore for salt and heat transport, we use salinity and temperature coordinates respectively. Details for calculating TEF from a numerical model are given in Lorenz et al. (2019) and discussed in the Supporting Information S1. All TEF output is calculated here using the pyTEF library (Lorenz et al., 2020). We calculate TEF values on 7 transects along SF fjord (Figure 1). For the time series of TEF transport, we show the transport at the 3rd line (SF Line 3).

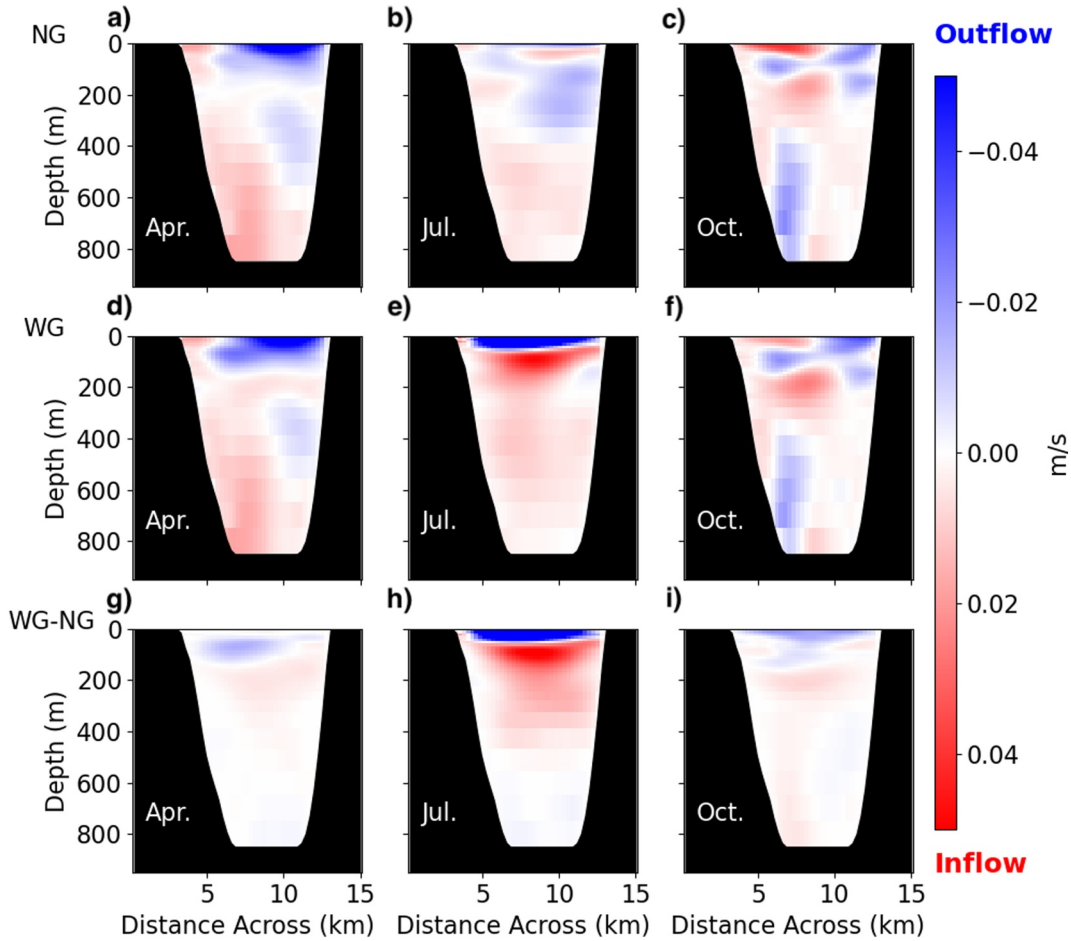

Figure 7. (a–c) monthly averages of velocity at SF Line 3 in April, July and October for the No Glacier (NG) run (d–f) in April, July and October for the West Glacier (WG) run. Positive velocities are flowing into the fjord. The view is downfjord with 0 km to the west.

5.2. Depth Coordinates Exchange-Flow Structure

Prior to using TEF, we evaluate the temporal variability of the exchange flow in traditional depth coordinates. The transport per depth at SF Line 3 for the NG run is shown in Figure 11a. With 3 years of data, a picture emerges of seasonal volume transport in the fjord with a reversing circulation below 200 m (Figure 11a). The transport is filtered with a 30-day rolling mean to remove the first-order synoptic variability associated with the winds. The transport is roughly in two layers below 200 m (Figure 11). The circulation is inflowing at depth in the spring and reverses to outflowing during the summer. This circulation is interrupted, especially in the upper 200 m, by the cumulative effects of wind events that are not completely filtered out. The seasonal cycle dominates over interannual variability.

The isolated plume-driven transport (the WG run with the NG run subtracted) shows a strong seasonal cycle with an increase in outflow during the summer and a compensating inflow between 200 and 500 m (Figure 11b). The primary outflow depth appears to rise and fall each summer consistent with a neutral buoyancy depth that is based on the magnitude of subglacial discharge.

5.3. Density Coordinates Exchange-Flow Structure

Applying TEF to SF line 3 enables us to calculate the seasonal volume transport of the fjord in density space (Figure 12) and allows direct connection with water mass variability. The composite TEF analysis shows that the NG transport is generally concentrated in the most dense layers. During the first half of the year, the deep flow is positive with inflow at depth and outflow at lighter densities. As seen in depth space (Figure 11), the flow reverses

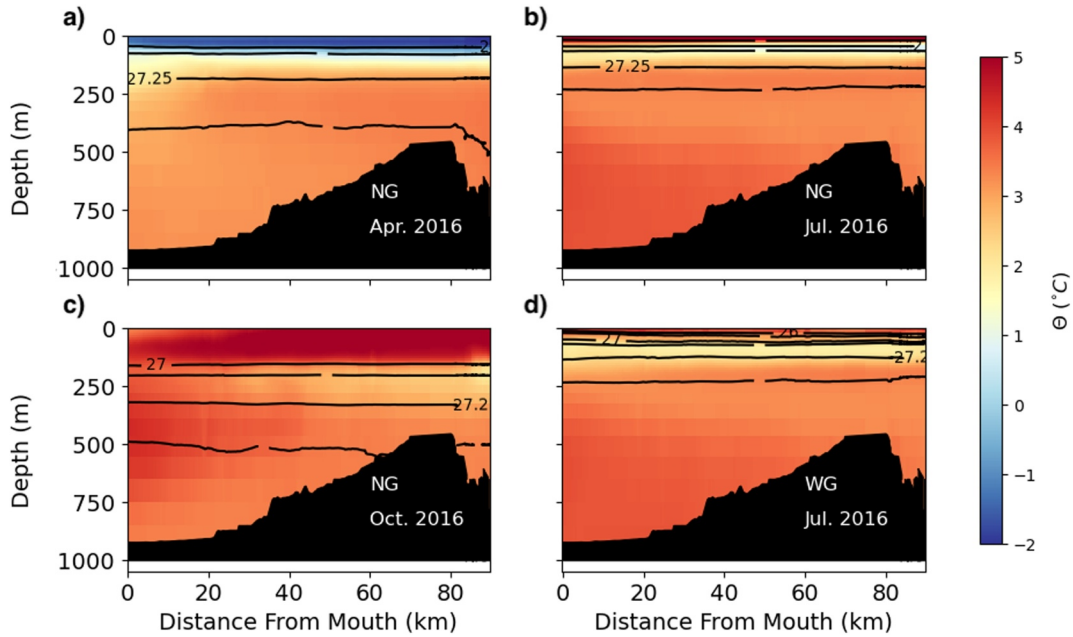

Figure 8. Width-averaged monthly temperature in April (a) and July (b) and October (c) for the No Glacier (NG) run and July (d) for the With Glacier (WG) run. The contours are isopycnals of potential density anomaly (26, 27, 27.15, 27.35, 27.45 kg/m^3). The transect in Figure 7 is located at 30 km.

in the second half of the year. Upon closer inspection, the inflowing density from January to June can be seen to be getting progressively denser filling the fjord with a greater concentration of AW. When the exchange reverses, the outflowing deep water can be seen getting progressively lighter. The WG circulation stands out in the summer and it overtakes the background NG circulation (Figure 12). The inclusion of the plume alters the total circulation

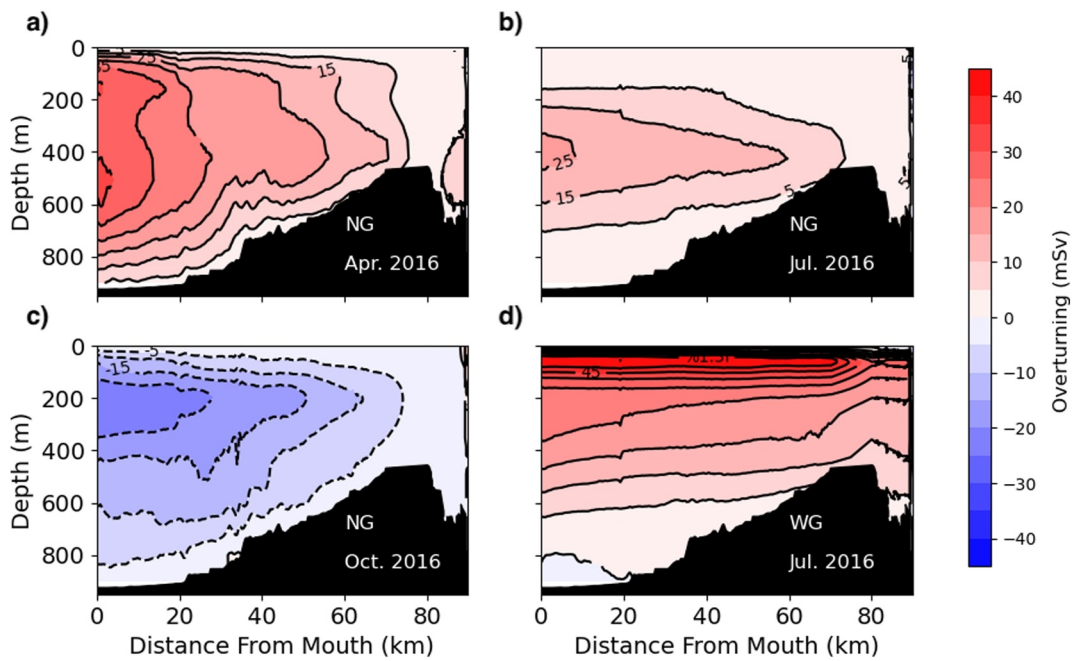

Figure 9. The streamfunction reverses between April and October in the No Glacier (NG) run. Width and monthly-averaged overturning streamfunction over April, July and October (NG), and July (With Glacier) in 2016. Counter-clockwise flow is a positive streamfunction.

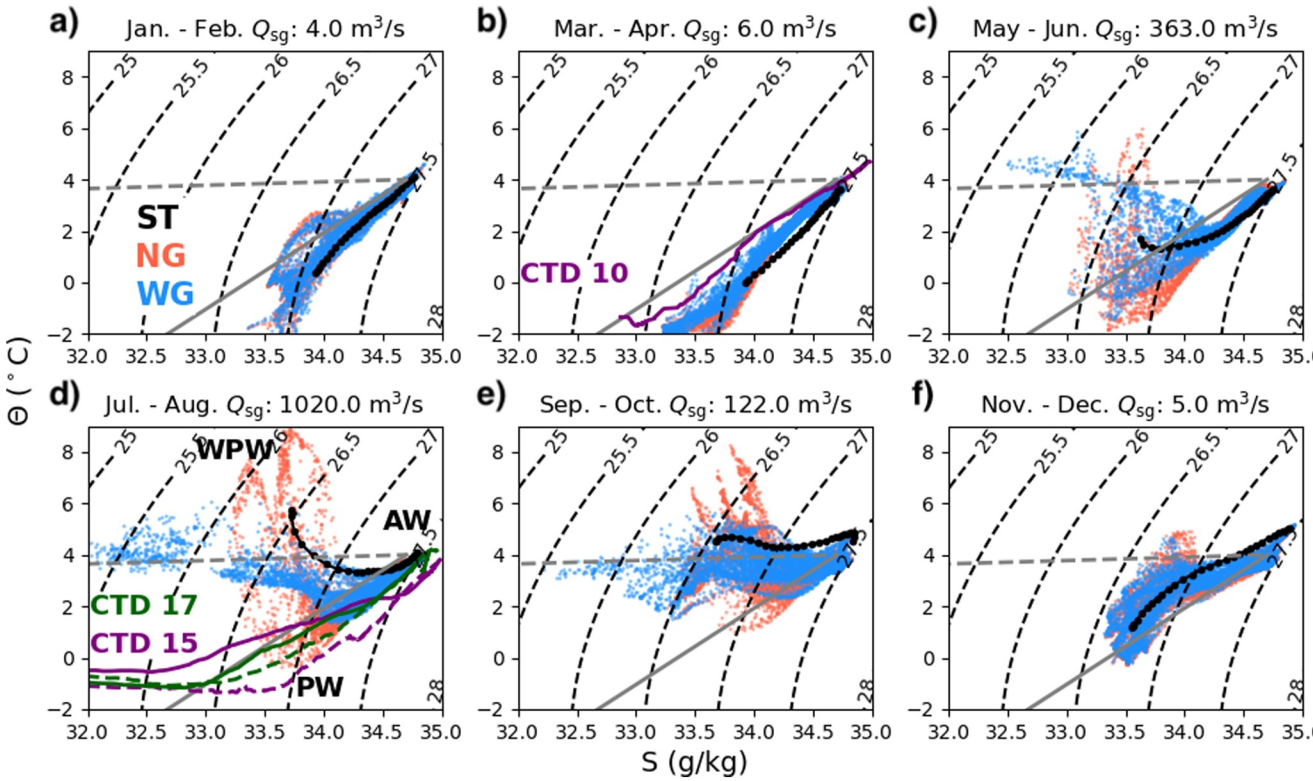

Figure 10. Each panel shows the T-S properties over a 2-month period with the spread coming from time (daily) and depth. The data come SF line 3. The blue dots are from the With Glacier (WG) run and the red dots are from the No Glacier (NG) run. The black dotted line is the T-S properties in Sermilik Trough (ST) in the NG run. The gray solid line is the melt-mixing line and the gray dashed line is a subglacial-discharge-mixing line. The contours are potential density anomaly. Q_{sg} is the 2-month average subglacial discharge. The spatial average (not including depth) from all CTD profiles (Figure 1) in August 2015 (purple, CTD 15), July 2017 (green, CTD 17), and March 2010 (purple, CTD 10) are included. We separately average profiles collected on the shelf (dashed) from those collected within the fjord (solid). The water mass locations are labeled in panel d.

enough to prevent the deep reversal from occurring until later in the fall. The TEF composite profiles also highlight the multi-layered exchange occurring in SF (Figures 11 and 12). In the winter months, there are multiple zero crossings separating the outflowing and inflowing cores at 27 kg/m^3 and 27.3 kg/m^3 respectively. The multiple inflows raise questions as to the physical meaning of TEF terms such as S_{in} or S_{out}. With this caution in mind, our analysis of TEF bulk values will assume they are representative of a larger 2-dimensional overturning circulation.

5.4. Exchange Flow Connections With Wind Stress

The exchange flow reversal exports AW (Figures 10 and 12) and is therefore an important lever in reducing the heat available to melt. We propose that the seasonality of the winds is responsible for the reversal by flattening isopycnals across the shelf during the spring. The mean state of the winds along the shelf is consistently downwelling favorable, such that a relaxation toward no winds acts effectively as upwelling. The changing slope of isopycnals in Sermilik Trough are qualitatively consistent with this picture (Figure 5).

The relationship between low-frequency wind forcing and the exchange reversal is tested by comparing the time derivative of low-pass along-shelf wind stress (τ_{lp}) and the TEF density exchange (Figure 13). Both of these variables are related to the change in pycnocline depth: if the density exchange is negative, then the fjord is getting lighter (pycnocline deepening). The density exchange is represented by $\Delta\sigma = \sigma_{in} - \sigma_{out}$ from the NG run at SF Line 3. Rather than use the 30-day running mean, we use a 90-day low-pass filter to calculate $\Delta\sigma$ to be consistent with τ_{lp}. The goal of this filter is to reduce synoptic forcing since we are interested in the change in exchange flow direction on longer timescales. When $\Delta\sigma > 0$, the exchange flow is positive with inflow at depth. The derivative of the seasonal wind stress is significantly correlated with $\Delta\sigma$ ($r = 0.68$) suggesting that wind variability is consistent

with the exchange flow. The seasonal variability of wind stress therefore likely plays an important role in setting the amount of AW in SF with relaxing winds leading to a greater concentration of AW.

5.5. Variability of TEF Bulk Properties

We quantify the TEF exchange volume transport as

$$Q_e = \frac{Q_{in} - Q_{out}}{2}, \quad (1)$$

where Q_{in} is the TEF inflowing volume transport (calculated in density space) and Q_{out} is the outflowing transport with $Q_e \geq 0$ (MacCready et al., 2018). In the NG run, the cycle of the exchange flow is consistent with the seasonal cycle of wind forcing with the greatest exchange occurring during the winter months (max 60 mSv) and weak exchange during the summer (max 10 mSv) (Figure 14a). The exchange flow in the WG run diverges from the NG run during the summer with peak exchange around 40 mSv. Since the plume forcing is strongest in the summer when the shelf-driven circulation is weakest, the exchange exceeds 30 mSv for the majority of the year. In the WG run, the exchange minimum is found in the non-summer months and varies from year to year depending on wind strength. In 2015 and 2016 the minimum occurs in November after the plume has shut off and during a relatively weak period of winds, but in 2017 the minimum occurs in March.

To isolate the plume forcing against the background shelf forcing, we separate the exchange flow into the plume-driven exchange (WG-NG) and shelf-driven exchange (NG). The plume-driven exchange peaks in July and the timing coincides with the input of subglacial discharge (Figure 3b).

We compare the shelf-driven exchange (NG) with coastal-trapped wave (CTW) theory (Equation B1). The application of the theory is described in Appendix B, but essentially estimates a volume transport based on pycnocline fluctuations. Forcing other than CTW exists in the NG run, but we use the CTW theory as a first-order approximation of the exchange flow. The exchange flow predicted by variation in pycnocline depth is correlated with the NG exchange flow ($r = 0.48$, Figure 14c). However this is because both transports peak in winter. Individual peaks in the CTW theory do not necessarily align with peaks in the NG transport. The theory suggests minimal impact of CTWs in summer when there is still an exchange on the order of 20 mSv. Clearly, additional factors are influencing the exchange in the NG run, but the comparison indicates that CTW dynamics can be a significant contributor to the background exchange flow.

Subglacial discharge drives a large salt exchange and export of freshwater onto the shelf (Figure 14d). The salt exchange is defined as $Q_e \Delta S$ where $\Delta S = S_{in} - S_{out}$, with Q_e calculated using salinity coordinates. When $\Delta S > 0$, the exchange flow is positive with inflowing salty water at depth and the export of fresher water. The plume is the largest seasonal driver of the salt exchange with the WG run salt transport peaking during the summer (Figure 14d). In the absence of subglacial discharge forcing, the salt exchange is relatively weak during the summer. The rest of the year the salt transport is variable due to wind forcing, but is generally negative in the fall and positive during the winter when the circulation reverses.

The heat exchange is defined as $Q_e \Delta\Theta \rho c_w$ where $\Delta\Theta = \Theta_{in} - \Theta_{out}$, c_w is the specific heat capacity of seawater and Q_e is calculated in temperature coordinates. When $\Delta\Theta > 0$, the exchange flow is positive with inflowing warm water at depth and the export of cooler water. The heat exchange is dominated by the shelf-driven circulation (Figure 14e) and therefore fluctuates between positive and negative depending on wind-strength. The addition of subglacial discharge results in a negative heat exchange in the WG run, that is the fjord is exporting heat, but this transport is small in comparison to the larger fluctuations in the winter.

In summary, the TEF results and shelf-plume forcing comparison indicate that the timing of subglacial discharge results in a strong exchange flow when the shelf-driven circulation $\left(Q_e^{NG}\right)$ is relatively weak. The peaks in shelf and plume-driven circulation ($Q_e^{WG} - Q_e^{NG}$) are consistent with the timing of subglacial discharge and CTWs lending confidence to our understanding of the drivers of the exchange flow. The salt exchange in the WG run consistently peaks in the summer, while both the heat and salt transport in the winter are more variable.

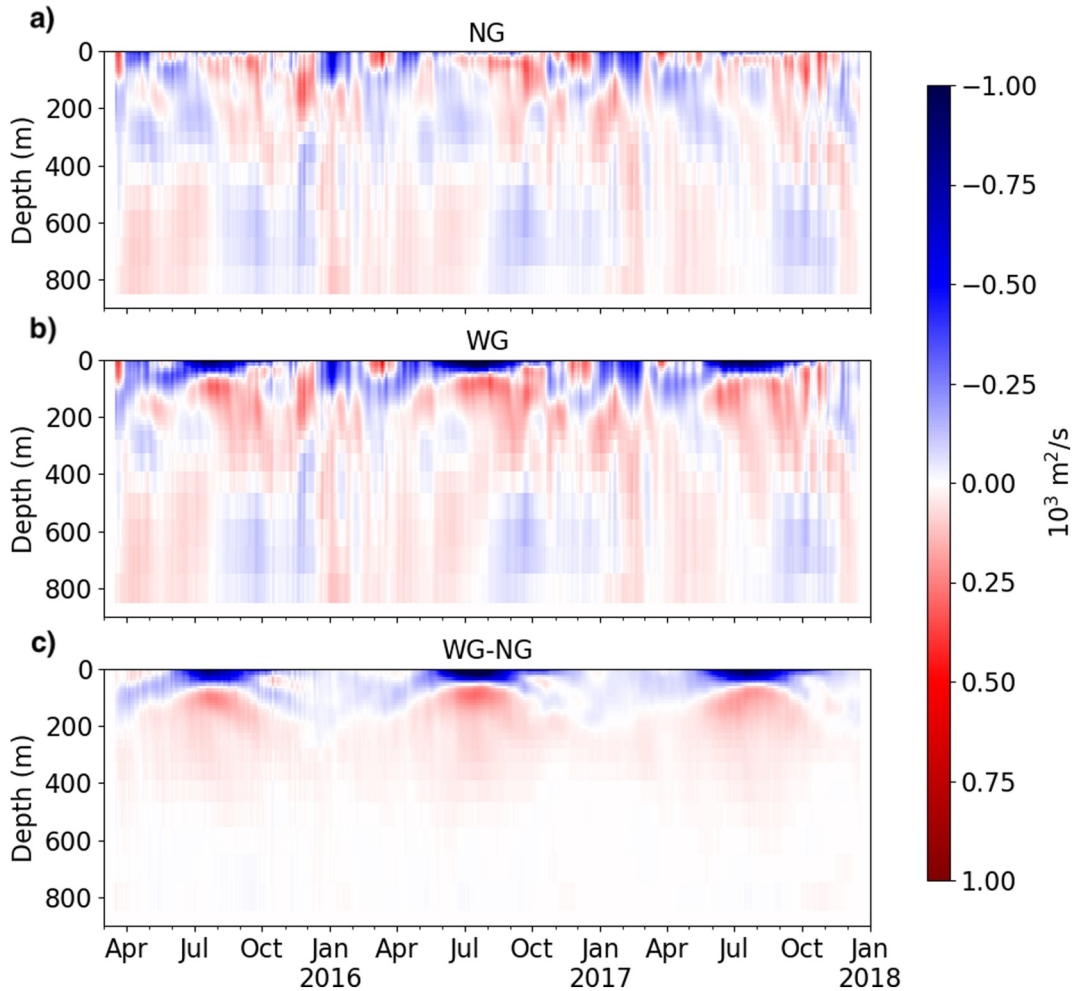

Figure 11. (a) 30-day rolling mean volume transport per meter in the No Glacier (NG) run at SF line 3 as a function of depth and time. Positive transport is into the fjord. (b) Same as (a) but for the With Glacier (WG) run. (c) The difference between the volume transport per meter in the WG run and the NG.

5.6. Along-Fjord Variability of Q_e

Given the different forcing source locations, we expect the shelf-driven circulation and plume-driven circulation to produce different along-fjord variability. The differences between the WG and NG run is most pronounced in the summer when the plume-driven circulation is greatest and shelf-driven circulation is weakest. The shelf-driven circulation, active in non-summer months, is most intense at the mouth of the fjord and decays with distance (Figure 15a). In contrast, the plume-driven circulation in summer (June–August) decays only slightly as it flows down the fjord. For a long fjord such as SF, the magnitude of the shelf-driven circulation has been reduced by 66% 70 km upfjord while the plume-driven circulation is most intense near the terminus where entrainment is high (5–10 km).The bulk TEF properties S_{in} and S_{out} are nearly constant along the length of the fjord (Figure S7 in Supporting Information S1) suggesting that vertical mixing is weak in the fjord interior.

The flushing time V/Q_e is defined as the volume upfjord of a section divided by the exchange flow and is a scaling for residence time within the fjord. The flushing time when the shelf-driven circulation dominates (Winter, Spring, Autumn) is always longer than the flushing time in summer and only decreases to between 100–150 days (Figure 15b). The plume-driven circulation flushing time is similar to winter near the mouth of the fjord, but drops

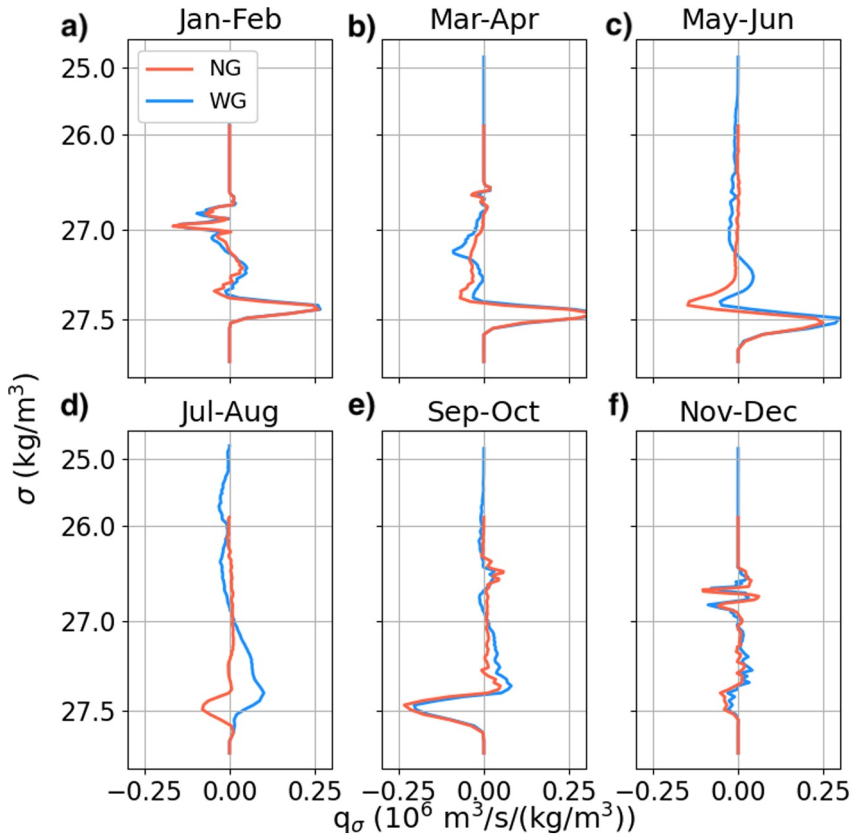

Figure 12. The Atlantic Water (AW) inflow ($\sigma \sim 27.4$ kg/m^3) becomes progressively denser until July and then reverses becoming progressively lighter. Each panel is a 3-year average over the 2 months evaluated at SF Line 3. The x-axis is q_σ volume transport per density class. The y-axis is potential density anomaly σ. Note the y-axis is nonlinear so that greater resolution can be given to the deepest densities. Red is from the No Glacier run, and blue is from the With Glacier run. 50 density bins were for used this figure instead of 1,000 for clarity.

linearly toward the head resulting in a flushing time of 50 days closer to Helheim Fjord. The contrasting along-fjord slopes suggests the plume-driven circulation is more effective at renewing the fjord than the shelf-driven circulation. This flushing time is meant to provide a scaling for residence time within the fjord, and we note other residence time scalings such as the freshwater fraction method produce different residence times, but a qualitatively consistent picture.

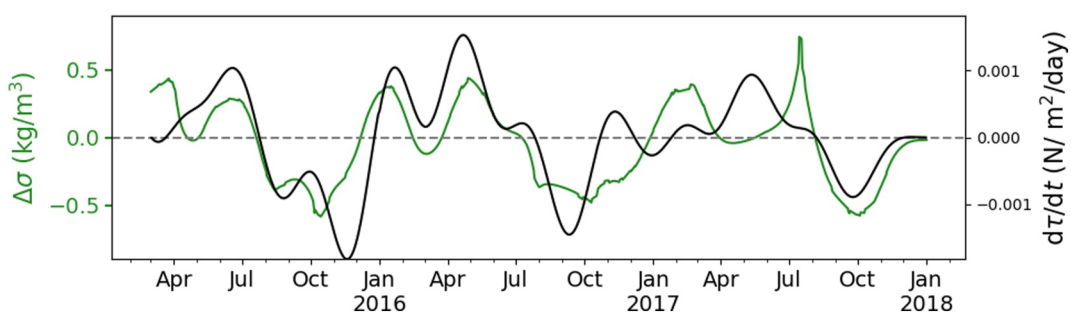

Figure 13. Flow reversals are correlated with changing wind stress. In green (left axis) is the difference between the Total Exchange Flow calculated σ_{in}, σ_{out} at SF line 3 calculated with a 90-day low-pass filter. Positive indicates inflow at depth. The data come from the No Glacier run. The right axis (black) is the derivative of the (90-day low-pass) along-shelf wind stress.

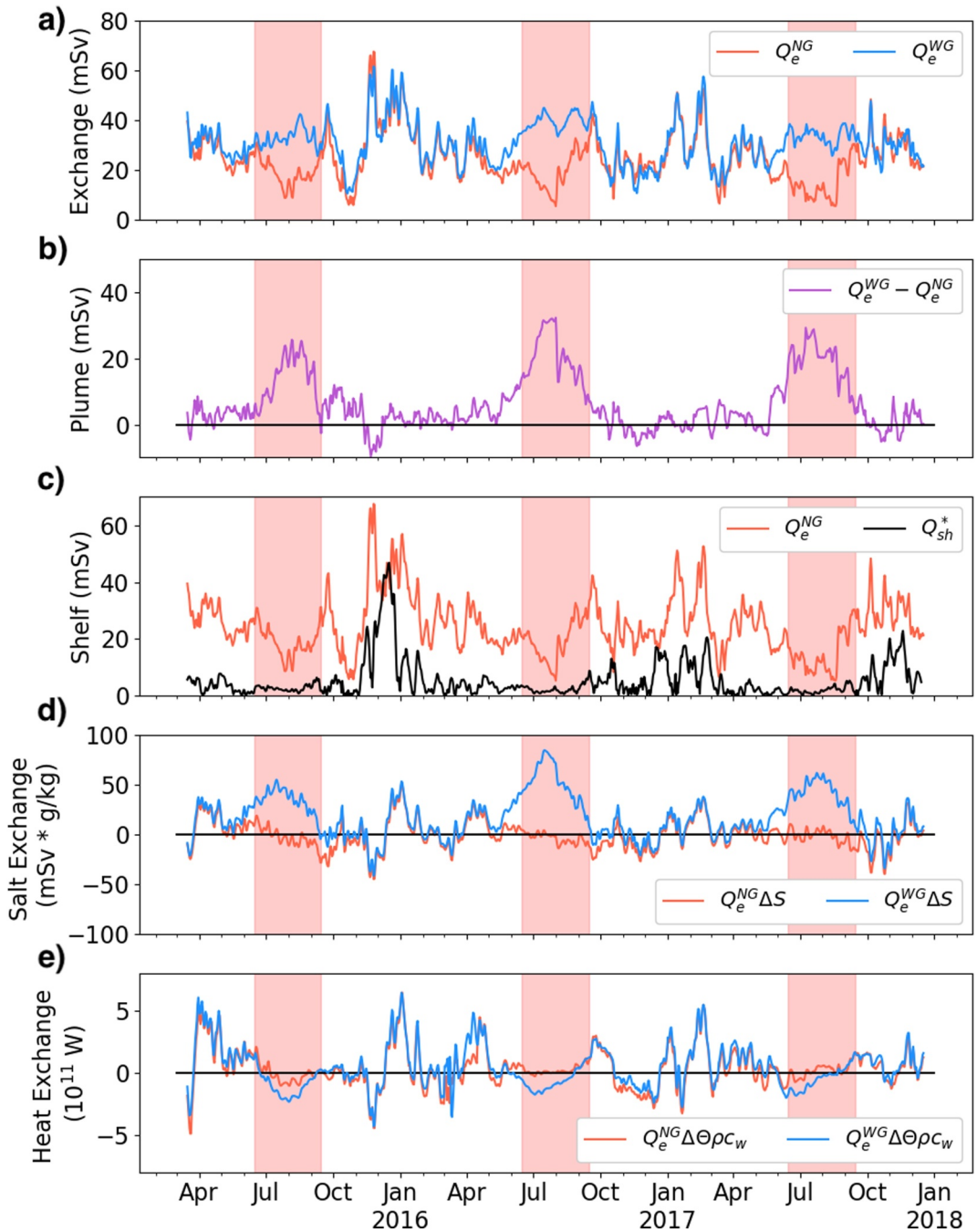

Figure 14. The shelf-driven and plume-driven exchange flows have peaks during the winter and summer months, respectively. (a) Exchange flow at SF line 3 in the No Glacier (NG) and With Glacier run. Units are in mSv (10^3 m^3/s). Red shading indicates summer period (June 15–September 15). (b) The difference between the WG and NG runs at SF line 3. (c) Exchange flow estimated from coastal-trapped waves (Jackson et al., 2018) and the NG run. (d) Salt transport from the exchange flow. The black line separates positive (incoming salt) from negative salt transport. (e) Heat transport from the exchange flow. Positive heat transport would make the fjord warmer.

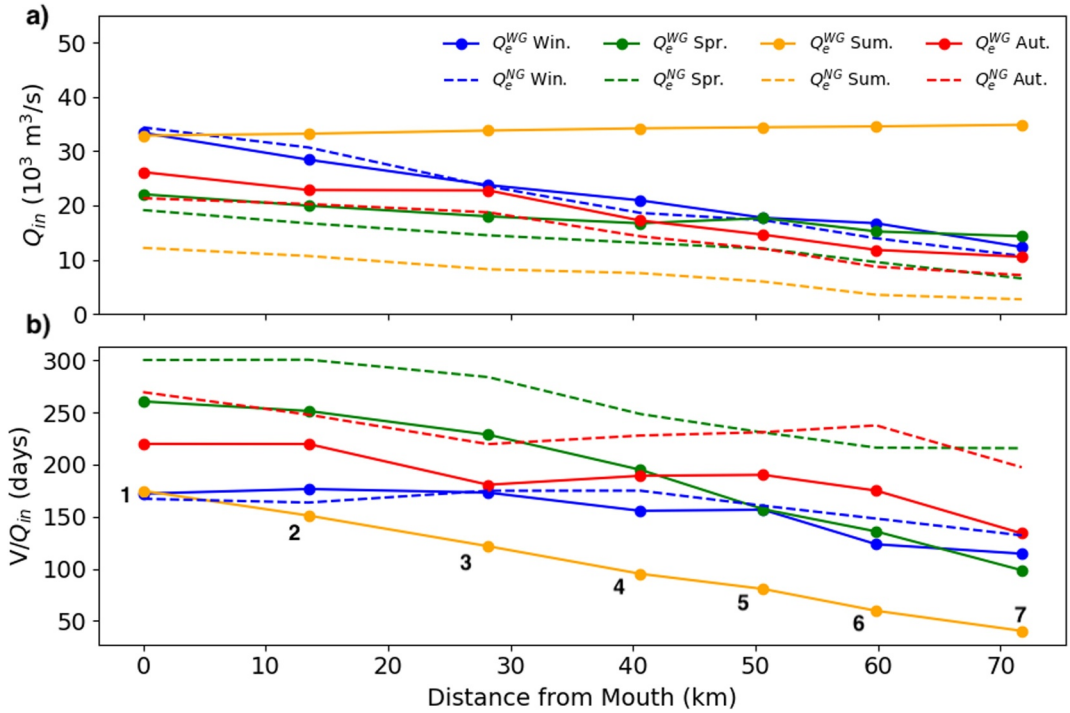

Figure 15. (a) Along-fjord Total Exchange Flow (TEF) exchange flow in 2016. Seasons are averages. The solid lines are from the With Glacier (WG) run and the dashed lines are from the No Glacier (NG) run. (b) A flushing time consisting of the fjord volume upfjord of a section divided by the exchange flow. The summer NG run flushing time is not included but is over 500 days at the mouth. Win is Winter (January–February), Spr. is Spring (March–May), Sum. is Summer (June–August), Aut. is Autumn (Fall, September — November). The locations of the markers are the cross-sections from Figure 1.

6. Discussion

6.1. Warm-Water Seasonality

Identifying the heat content variability of glacial fjords is essential given the sensitivity of submarine melting to warm water. An increase in fjord heat content can be driven by an increase in AW temperature or by an increase in the relative concentration of warm AW to cold PW. We find that the vertically-averaged temperature of the fjord, and thus vertically-averaged thermal forcing, peaks in the fall (Figures 5 and 8). The temperature maximum in the fall is a result of both warm warm intruding into the fjord near the surface and seasonally-warmed AW advecting into the fjord at depth and is consistent with observations (Harden et al., 2014; Sutherland et al., 2013). However, we find that the greatest volume ratio of AW to PW, defined roughly from the height of the 27.3 kg/m^3 isopycnal, occurs in July as a result of relaxing isopycnals. Therefore, these two warming mechanisms have different seasonal patterns (Figure S10 in Supporting Information S1). A warming of the Irminger Sea would result in a larger temperature anomaly at depth in fall, while a reduction in along-shelf winds would increase the thickness of the AW layer and result in a larger temperature anomaly in spring or summer. However, fjord circulation and its seasonality will modify the amount of oceanic heat that ultimately reaches the glacier. For example, while the temperature remains relatively constant along the fjord, volume transport is not. Consequently, the oceanic heat transport decays if it is shelf-driven but remains nearly constant if it is plume-driven (Figure 15). The impact of external heat on glaciers will depend on iceberg concentration, the mechanism of fjord heat transport, and processes at the ice-ocean interface, which are still poorly understood.

We would also like to point out that the inclusion of substantial submarine melting (e.g., from icebergs) is likely to change the heat exchange interpretation during the summer. In the WG run, the heat exchange is negative during the summer as a result of upwelled AW and a shallow outflowing plume (Figure 8d). If the upper-layer was properly cooled, we would observe a positive heat exchange. A steady and positive heat exchange would be consistent with observations (Jackson & Straneo, 2016). As the streamfunction shows (Figure 9d), the plume-driven circulation drives transport between 200 and 500 m all the way toward the glacier, and therefore,

increased subglacial discharge should lead to increased heat transport and greater melting of both the terminus and icebergs. Inclusion of melting could then lead to a feedback with an increased buoyancy-driven circulation (Kajanto et al., 2023; Zhao, Stewart, & McWilliams, 2022). To explore this question fully, more realistic melting needs to be included in numerical models (Schulz et al., 2022).

6.2. Relationship Between Glacial Stability and Shelf Forcing

Warmer ocean and atmospheric temperatures have been linked to increased glacial retreat in east Greenland (Straneo et al., 2011; T. R. Cowton et al., 2018). In SF, glacial retreat has also been correlated with the negative phase of the North Atlantic Oscillation (NAO) index (Andresen et al., 2012, 2014), the dominant mode of atmospheric climate variability in the North Atlantic related to pressure differences between Portugal and Iceland. A negative NAO index is associated with increased AW content relative to PW, leading to increased heat transport across the shelf (Christoffersen et al., 2011). The positive phase of the NAO index is correlated with increased wind stress on the east Greenland coast (Harden et al., 2011). This can be seen in our model, as the NAO was more positive during the winter of 2015–2016 than the winter of 2016–2017. Despite increasing shelf-driven circulation within fjords, the positive phase is correlated with glacial stability (Andresen et al., 2014). Our model is consistent with this correlation, as we find that under reduced downwelling winds, shelf isopycnals flatten and the fjord-shelf exchange promotes an increase in AW. This mechanism has recently been observed on shorter timescales (1–10 days) using satellite observations (Snow et al., 2023). Therefore, our results extend into the fjords the dynamical connection between large-scale wind variability and heat transport across the shelf (Christoffersen et al., 2011). We find the seasonality and direction of the along-shelf winds play an important role in setting oceanic thermal forcing of the glacier.

6.3. Implications for Fjord Renewal

While the seasonality of the along-shelf winds play an important role in increasing the heat content in SF, we find that the circulation induced from shelf forcing decays away from the mouth and has a reduced effect closer to the fjord head. In contrast, the plume-driven circulation in summer is capable of driving renewal across the whole length of the fjord. Therefore, we would expect fjord properties (e.g., heat, nutrients) close to the terminus to have the quickest renewal rates in summer when subglacial discharge is strongest. Additionally, near-terminus circulation is an important control of glacial melt rates. In large fjord systems such as Sermilik, the shelf-forced circulation decays limiting the direct effects of storms and shelf winds on submarine melting.

6.4. Fjord Mixing

There appears to be weak mixing in the main channel of Sermilik Fjord. TEF bulk properties of Salinity and Temperature (Figures S6 and S7 in Supporting Information S1) are nearly constant along the fjord. During the winter, even though CTWs can drive a rapid fluctuation, they might contribute only modestly to mixing. Low dissipation would be consistent with modeling studies focusing on CTWs on Greenland's shelf and fjords (Gelderloos et al., 2021, 2022). During the summer, when the circulation is plume-dominated, the weak mixing indicates that the outgoing exchange is primarily set by the subglacial discharge plume parameterization. The addition of icebergs is likely to add additional mixing downfjord and would be consistent with some observations (Muilwijk et al., 2022).

7. Conclusion

Glacial fjords are critical to the climate system by exchanging heat and salt between the ice sheet and open ocean. We analyzed the output from two three-year simulations of a glacial fjord with realistic forcing. One simulation included glacial and shelf forcing (WG) while the other only included shelf forcing (NG), allowing us to identify the relative roles of shelf and plume forcing on shelf-fjord exchange. Using the NG run, we found that the shelf forcing was able to drive significant exchange even in the absence of glacial forcing. Additionally, we found that the sign of the exchange flow is related to the seasonality of the along-shelf wind stress which controls the across-shelf isopycnal gradients. When downwelling winds subside, shelf isopycnals flatten and the fjord fills with warm AW in the summer. In SF, the minimum of the along-shelf wind stress happens to coincide with peak glacial forcing generating two distinct regimes, a shelf-driven circulation in non-summer months with variable heat and salt exchange, and a plume-driven circulation in the summer with a large salt exchange. The plume-driven exchange

shows little along-fjord variability and is more effective at renewing tracers than the shelf-driven circulation which peaks at the fjord mouth. Therefore, the direct effect of the shelf-driven circulation on driving melt-rate variability is likely secondary to thermal forcing. Key limitations of this study are a parameterized ice face which produces weak melting outside of the plume and a lack of icebergs which are likely a considerable heat sink in the fjord.

Appendix A: Model and Data Comparison

A1. Observational Data

The model runs presented in this paper are some of the first multi-year simulations of a Greenland glacial fjord with realistic atmospheric and oceanic forcing. Evaluation and comparison of the model against observations is limited to a selected number of moorings, although these moorings span different regions of the fjord-shelf system (Figure 1). We compare the model to three moored Conductivity, Temperature and Depth (CTD) instruments

Table A1
Moored Observations and CTDs From 2015–2017

Label	Instrument	Depth	Deployment time	Sample resolution	Variables
CM6	SBE 37 MicroCAT	350 m	August 2013–August 2016	15 min	Θ, *S*, *P*
CM0	SBE 37 MicroCAT	60 m	August 2015–July 2017	15 min	Θ, *S*, *P*
SF4	SBE 37 MicroCAT	400 m	August 2015–July 2017	15 min	Θ, *S*, *P*
SF6	SBE 37 MicroCAT	350 m	August 2015–July 2017	15 min	Θ, *S*, *P*
SF4 ADCP	75 kHz RDI Teledyne Workhorse Long-ranger ADCP (Upward facing)	381–41 m (10 m bins)	August 2015–July 2017	30 min	*V*
OW1 ADCP	75 kHz RDI Teledyne Workhorse long-ranger ADCP (Upward facing)	143–18 m (5 m bins)	August 2015–July 2017	30 min	*V*
CTD 2015	SBE 25plus MicroCAT	Full depth	August 2015	1 m	Θ, *S*,*P*
CTD 2017	SBE 25plus MicroCAT	Full depth	July 2017	1 m	Θ, *S*,*P*

Note. Θ is Conservative Temperature, *S* is absolute salinity, *P* is pressure, *V* is velocity.

(Table A1) from August 2015 to July 2017 located on the shelf at 350 m and in the fjord at 60 and 400 m (Figure 1). We also compare the model output to moored Acoustic Doppler Current Profiler (ADCP) velocity data collected in the fjord and on the shelf (Table A1). We compare the model output to 64 ship-based CTD profiles collected during summer surveys in 2015 and 2017. Lastly, we also include 4 winter XCTD profiles from March 2010 for additional context.

We evaluate the model using the Skill Score (Skill; Murphy, 1988) defined as

$$\text{Skill} = 1 - \frac{\frac{1}{N}\sum_{i=1}^{i=N}(m_i - o_i)^2}{\frac{1}{N}\sum_{i=1}^{i=N}(o_i - \overline{o})^2} = 1 - \frac{\text{MSE}}{\text{STD}_o^2}, \tag{A1}$$

where m_i is a model value, o_i is the observation value, the overbar denotes an average, MSE is the mean square error, STD is the standard deviation and there are N paired model and observation points. The Skill provides a metric for comparison across different model parameters, such as temperature and salinity, and is a commonly used tool when evaluating realistically forced models (e.g., Liu et al., 2009; Ralston et al., 2010; Sutherland et al., 2011). It can be shown that Skill = r^2-VB-MB, where r is the correlation coefficient, VB is the variance bias, and MB is the mean bias (Ralston et al., 2010; Sutherland et al., 2011) and thus the score evaluates the data across multiple dimensions. A Skill = 1 indicates perfect agreement between the model and observations, but in general a Skill above 0.2 is considered good.

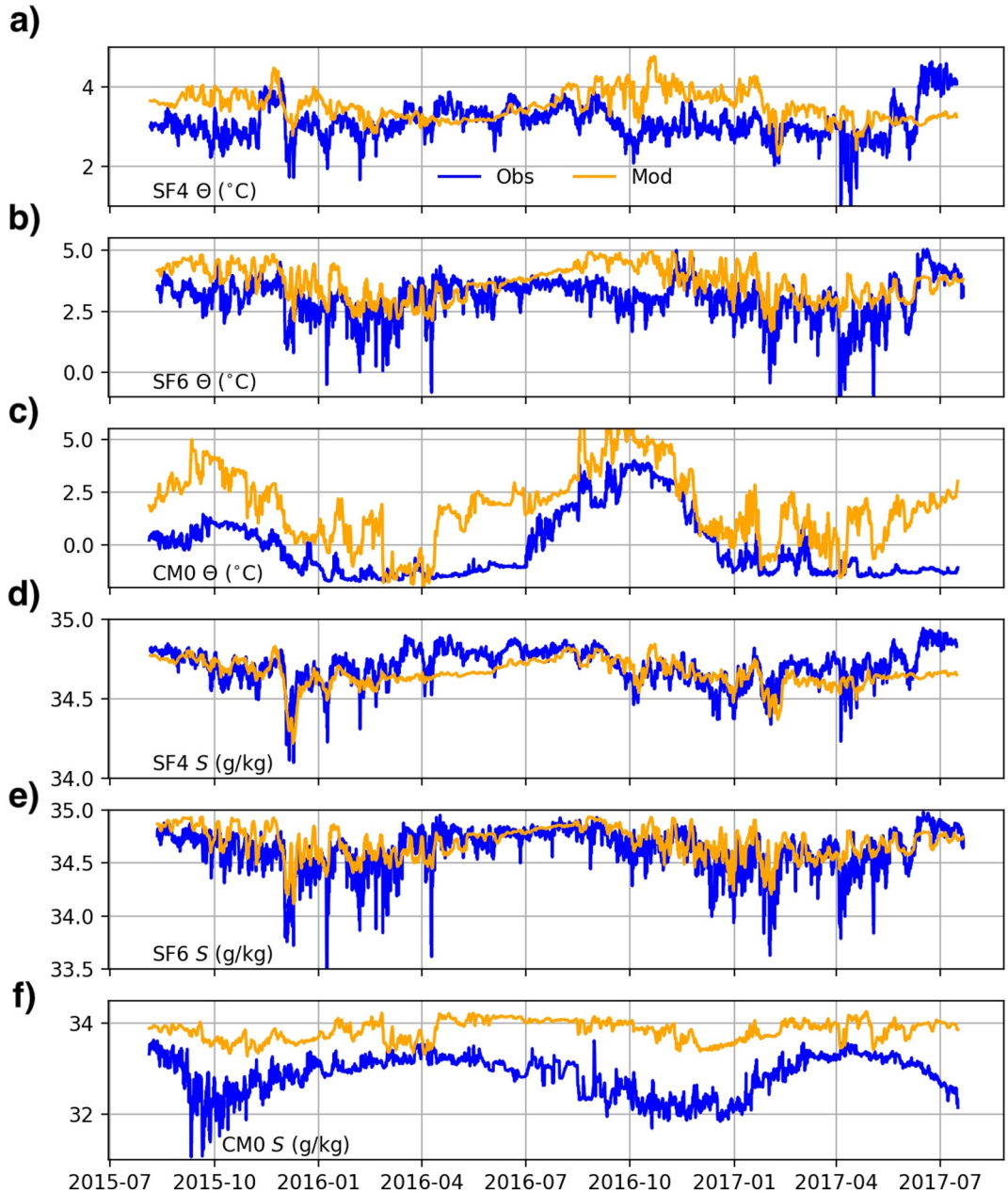

Figure A1. The model output (orange) reproduces shelf observations (blue), but cannot reproduce shallow fjord salinity. (a–c) are Conservative Temperature (Θ) at SF4, SF6, and CM0 at 400 m, 350 m, and 60 m respectively. (d–f) are Absolute Salinity (*S*) at SF4, SF6, and CM0.

We use *r* to diagnose the covariance between two variables. The statistical significance of the correlation coefficient is determined using the effective degrees of freedom defined as the e-folding scale of the autocovariance of the observations (Emery & Thomson, 2001; Lindeman et al., 2020).

A2. Model and Observation Comparison

To lend support that the model results are applicable to the real world Sermilik Fjord, we compare the WG model time series to 3 moored CTD instruments. The moored instruments recorded temperature and salinity on the shelf at 350 m and in the fjord at 60 and 400 m from August 2015–July 2017. The model boundary conditions were shifted in temperature and salinity to match the mean shelf mooring (CM6). The model appears to do a reasonable

job of recreating the seasonal temperature variability in the shallow part of the fjord ($r = 0.85$), but has a significant warm bias and a resulting weak Skill. The warm bias in the model PW during the summer was captured by the CTD profiles (Figure 10), but the model does a better job of capturing the cooler PW temperature in the winter (Figure A1c). The model is less capable of recreating surface salinity (Skill <0) and misses the large salinity minima which occur in the fall. The deeper moorings, especially the one on the shelf, do a better job of recreating salinity variability and temperature variability capturing both the minima in winter and the maxima in summer (Table A2, Figure A1).

Table A2
Statistics and Skill Scores for the Mooring Temperature, Salinity and Velocity Time Series

Variable	Skill_{lp}	MSE_{lp}	r_{lp}	Skill_{hp}	MSE_{hp}	r_{hp}
CM0 S	−6.0	1.1	0.42*	−0.13	0.03	0.13
CM0 Θ	−0.95	4.3	0.85*	−2.7	0.26	0.31
SF4 S	0.01	0.01	0.57*	0.12	0.003	0.50*
SF4 Θ	−1.8	0.40	−0.02	−0.33	0.08	0.21
SF6 S	0.33	0.02	0.75*	0.11	0.013	0.48*
SF6 Θ	−0.96	0.83	0.51*	0.05	0.23	0.41*

Note. The first column is the variable and mooring. Columns 2–4 are the Skill Score (Skill), Mean Square Error (MSE) and correlation coefficient (r) for the low-pass filtered time series, and columns 5–7 are statistics for the high-pass filtered time series. Significance is denoted with a star.

We compare the volume transport from the model with the transport calculated from the ADCP (Figure S2 in Supporting Information S1). Splitting the transport into seasons, the observed transport and standard deviation in the summer months (June–August) is 74 ± 26 mSv (10^3 m^3/s) and non-summer months (October–May) is 26 ± 7.7 mSv. The modeled transport is 33 mSv in summer and 36 mSv in the non-summer; both are within 1.6 standard deviations of the observed transport. Although the model transport appears to be underestimating transport in the summer. This underestimate is potentially driven by a lack of iceberg melt which has been shown to increase circulation by at least 10% (Davison et al., 2020).

A3. Summary Statistics

A table of Skill, r and MSE are given in Table A2. We don't calculate Skill or r scores for the ADCP at SF4 since the observed transport is an estimate and not directly measured. We isolate seasonal from synoptic (1–10 days) forcing by splitting all the data up into two time series: a low-pass time series y_{lp} generated from a 30-day low pass 6th order Butterworth filter and a high-pass time series $y_{hp} = y - y_{lp}$ generated from removal of the low-pass series from the original data. Most of the Skill are poor, and we can attribute this largely to differences in the MSE. The highest Skill are for the deep salinity (SF4 and SF6) where the model was shifted to reduce the mean bias. The skill scores tend to improve when looking at shorter timescales (<30 days) indicating the model is doing better at capturing wind-driven variability than the larger scale variability, a bias we attribute to lacking iceberg melt.

Appendix B: Contribution of CTWs to Shelf-Driven Circulation

Both Fraser et al. (2018) and Jackson et al. (2018) have identified coastal-trapped waves (CTWs) as the primary mechanism through which the wind-driven forcing is communicated to southeast glacial fjords, and CTWs have been observed in other dynamically-wide Arctic Fjords (Inall et al., 2015). We evaluate the contribution of CTWs to the shelf-driven circulation by comparing the model output with an analytical model of CTWs. For our analysis, we use the Kelvin-wave model from Jackson et al. (2018) who showed that Kelvin waves were a good representation of coastal-trapped waves in Greenland's fjords due to their steep sides. The Kelvin-wave model uses a two-layer approximation with the volume transport in the top layer given by

$$Q_{ctw} = 2cR_d\left(1 - e^{-W/R_d}\right)\sin\left(\frac{\omega}{c}(L + W/2 - y)\right)\eta(t), \quad \text{(B1)}$$

where η is the amplitude of the pycnocline fluctuation at the mouth, y is the distance from the mouth, ω is the forcing frequency, c is the baroclinic wave speed, L is the fjord length, W is the fjord width and R_d is the deformation radius $R_d = c/f$ where f is the Coriolis frequency. For our application, $c = \sqrt{g'h'}$ where g' is the reduced gravity between the upper layer h_1 and the bottom layer h_2, and $h' = h_1 * h_2/(h_1 + h_2)$ is the effective height. The layer heights were calculated by solving for the depth of the zero crossing of the first horizontal normal mode at the fjord mouth (K. G. Hughes et al., 2018). On average, $c = 0.68$ m/s, but it varies between 0.5 and 0.9 m/s from winter to summer respectively. This speed is lower than observations (Jackson et al., 2014, $c = 1.1$ m/s). This difference is most likely attributable to weak model stratification compared to observations. We define pycnocline fluctuations as

$$\eta_M = \frac{\Delta\sigma}{\overline{\sigma_z}}, \tag{B2}$$

where σ is the potential density anomaly at the mouth of the fjord and $\overline{\sigma_z}$ is a 30-day rolling mean of the section-averaged vertical density gradient at the mouth.

Since the fjord experiences broadband forcing rather than a single forcing period, we follow Jackson et al. (2018) and Fourier transform η to a function of frequency $\hat{\eta}(\omega)$. If c were a constant, we could use Equation B1 to solve for $\hat{Q}_{ctw}(\omega)$, and then inverse Fourier transform to get $Q_{ctw}(t)$. Although c is not constant, its dominant variation is seasonal. Because this is much longer than the dominant forcing periods of interest, we can approximately solve for $Q_{ctw}(t)$. Specifically, we calculate a 2D matrix of $\hat{Q}_{ctw}(c,\omega)$ using constant values of $c = [0.4, 0.5, \ldots, 1.1]$ m/s. We then inverse Fourier transform $\hat{Q}$ and use a timeseries of $c(t)$ to interpolate across $Q_{ctw}(c, t)$ and recover a 1D time series. The calculated CTW volume transport is about 66% the magnitude of the high-frequency (<15 days) incoming volume transport (Figure S9 in Supporting Information S1) suggesting the CTW theory is slightly underestimating CTW transport or additional high-frequency variability is present.

We apply a 30-day rolling mean to average over synoptic variability. The resulting transport is the net volume transport in the top layer. If we treat the fjord as two layers, then we can assume this transport is balanced by an opposite transport in the other layer. Therefore, the incoming transport will switch between the top and bottom layers as the pycnocline fluctuates, and so the total incoming transport can be written as $Q^*_{sh} = |Q_{ctw}|$, where the star denotes analytical model and the subscript sh represents shelf forcing.

Data Availability Statement

We have archived the outputs from the two MITgcm simulations at K. Hughes (2023). To make file sizes manageable, the outputs have been subset to once per day and the region north of 65.4°N. Observational data is available from the Arctic Data center for SF4 (Straneo, 2024d), SF6 (Straneo, 2024b), OW1 (Straneo, 2024e), CM6 (Straneo, 2024a), CM0 (Straneo, 2024c), CTD 2015 (Straneo & Holte, 2018) and CTD 2017 (Straneo, 2021). A jupyter notebook to generate the figures is available at: https://github.com/bob-sanchez/Relative_Roles_JGR24.git.

Acknowledgments
We acknowledge Margaret Lindeman, Sarah Giddings, and Rebecca Jackson for helpful discussions and suggestions. We thank An Ngyuen for providing ASTE data. We thank Michael Wood and one anonymous reviewer for their helpful suggestions which improved the organization and content of the manuscript. All authors acknowledge funding from the Heising-Simons Foundation. We acknowledge the use of imagery (AMSR2) from the NASA Worldview application (https://worldview.earthdata.nasa.gov), part of the NASA Earth Observing System Data and Information System (EOSDIS). The views presented herein are those of the writer and do not necessarily represent the views of DoD or its components.

References

Adcroft, A., Hill, C., Campin, J.-M., Marshall, J., & Heimbach, P. (2004). Overview of the formulation and numerics of the MIT GCM. In *Proceedings of the ecmwf seminar series on numerical methods, recent developments in numerical methods for atmosphere and ocean modelling* (pp. 139–149).

Andresen, C. S., Schmidt, S., Seidenkrantz, M.-S., Straneo, F., Grycel, A., Hass, C. H., et al. (2014). A 100-year record of changes in water renewal rate in sermilik fjord and its influence on calving of Helheim glacier, southeast Greenland. *Continental Shelf Research*, *85*, 21–29. https://doi.org/10.1016/j.csr.2014.05.017

Andresen, C. S., Straneo, F., Ribergaard, M. H., Bjørk, A. A., Andersen, T. J., Kuijpers, A., et al. (2012). Rapid response of Helheim Glacier in Greenland to climate variability over the past century. *Nature Geoscience*, *5*(1), 37–41. https://doi.org/10.1038/ngeo1349

Aure, J., Molvær, J., & Stigebrandt, A. (1996). Observations of inshore water exchange forced by a fluctuating offshore density field. *Marine Pollution Bulletin*, *33*(1), 112–119. https://doi.org/10.1016/S0025-326X(97)00005-2

Beaird, N., Straneo, F., & Jenkins, W. (2018). Export of strongly diluted Greenland meltwater from a major glacial fjord. *Geophysical Research Letters*, *45*(9), 4163–4170. https://doi.org/10.1029/2018GL077000

Burchard, H., Bolding, K., Feistel, R., Gräwe, U., Klingbeil, K., MacCready, P., et al. (2018). The Knudsen theorem and the total exchange flow analysis framework applied to the Baltic Sea. *Progress in Oceanography*, *165*, 268–286. https://doi.org/10.1016/j.pocean.2018.04.004

Carroll, D., Sutherland, D. A., Curry, B., Nash, J. D., Shroyer, E. L., Catania, G. A., et al. (2018). Subannual and seasonal variability of Atlantic-origin waters in two adjacent west Greenland fjords. *Journal of Geophysical Research: Oceans*, *123*(9), 6670–6687. https://doi.org/10.1029/2018JC014278

Carroll, D., Sutherland, D. A., Shroyer, E. L., Nash, J. D., Catania, G. A., & Stearns, L. A. (2015). Modeling turbulent subglacial meltwater plumes: Implications for fjord-scale buoyancy-driven circulation. *Journal of Physical Oceanography*, *45*(8), 2169–2185. https://doi.org/10.1175/JPO-D-15-0033.1

Carroll, D., Sutherland, D. A., Shroyer, E. L., Nash, J. D., Catania, G. A., & Stearns, L. A. (2017). Subglacial discharge-driven renewal of tidewater glacier fjords. *Journal of Geophysical Research: Oceans*, *122*(8), 6611–6629. https://doi.org/10.1002/2017JC012962

Christoffersen, P., Mugford, R. I., Heywood, K. J., Joughin, I., Dowdeswell, J. A., Syvitski, J. P. M., et al. (2011). Warming of waters in an East Greenland fjord prior to glacier retreat: Mechanisms and connection to large-scale atmospheric conditions. *The Cryosphere*, *5*(3), 701–714. https://doi.org/10.5194/tc-5-701-2011

Cowton, T., Slater, D., Sole, A., Goldberg, D., & Nienow, P. (2015). Modeling the impact of glacial runoff on fjord circulation and submarine melt rate using a new subgrid-scale parameterization for glacial plumes. *Journal of Geophysical Research: Oceans*, *120*(2), 796–812. https://doi.org/10.1002/2014JC010324

Cowton, T. R., Sole, A. J., Nienow, P. W., Slater, D. A., & Christoffersen, P. (2018). Linear response of east Greenland's tidewater glaciers to ocean/atmosphere warming. *Proceedings of the National Academy of Sciences*, *115*(31), 7907–7912. https://doi.org/10.1073/pnas.1801769115

Davison, B. J., Cowton, T. R., Cottier, F. R., & Sole, A. J. (2020). Iceberg melting substantially modifies oceanic heat flux towards a major Greenlandic tidewater glacier. *Nature Communications*, *11*(1), 5983. https://doi.org/10.1038/s41467-020-19805-7

Emery, W. J., & Thomson, R. E. (2001). *Data analysis methods in physical oceanography* (revised 2nd ed.). Elsevier Science. https://doi.org/10.1016/B978-044450756-3/50007-1

Enderlin, E. M., Howat, I. M., Jeong, S., Noh, M.-J., Angelen, J. H. v., & Broeke, M. R. v. d. (2014). An improved mass budget for the Greenland ice sheet. *Geophysical Research Letters*, *41*(3), 866–872. https://doi.org/10.1002/2013GL059010

Ezhova, E., Cenedese, C., & Brandt, L. (2017). Dynamics of a turbulent buoyant plume in a stratified fluid: An idealized model of subglacial discharge in Greenland fjords. *Journal of Physical Oceanography*, *47*(10), 2611–2630. https://doi.org/10.1175/JPO-D-16-0259.1

Fraser, N. J., & Inall, M. E. (2018). Influence of barrier wind forcing on heat delivery toward the Greenland ice sheet. *Journal of Geophysical Research: Oceans*, *123*(4), 2513–2538. https://doi.org/10.1002/2017JC013464

Fraser, N. J., Inall, M. E., Magaldi, M. G., Haine, T. W. N., & Jones, S. C. (2018). Wintertime fjord-shelf interaction and ice sheet melting in southeast Greenland. *Journal of Geophysical Research: Oceans*, *123*(12), 9156–9177. https://doi.org/10.1029/2018JC014435

Gade, H. G. (1979). Melting of ice in sea water: A primitive model with application to the Antarctic ice shelf and icebergs. *Journal of Physical Oceanography*, *9*(1), 189–198. https://doi.org/10.1175/1520-0485(1979)009⟨0189:MOIISW⟩2.0.CO;2

Gelderloos, R., Haine, T. W. N., & Almansi, M. (2021). Coastal trapped waves and other subinertial variability along the southeast Greenland coast in a realistic numerical simulation. *Journal of Physical Oceanography*, *51*(3), 861–877. https://doi.org/10.1175/JPO-D-20-0239.1

Gelderloos, R., Haine, T. W. N., & Almansi, M. (2022). Subinertial variability in four southeast Greenland fjords in realistic numerical simulations. *Journal of Geophysical Research: Oceans*, *127*(11), e2022JC018820. https://doi.org/10.1029/2022JC018820

Gelderloos, R., Haine, T. W. N., Koszalka, I. M., & Magaldi, M. G. (2017). Seasonal variability in warm-water inflow toward Kangerdlugssuaq fjord. *Journal of Physical Oceanography*, *47*(7), 1685–1699. https://doi.org/10.1175/JPO-D-16-0202.1

Gladish, C. V., Holland, D. M., & Lee, C. M. (2014). Oceanic boundary conditions for Jakobshavn glacier. part II: Provenance and sources of variability of disko bay and ilulissat icefjord waters, 1990–2011. *Journal of Physical Oceanography*, *45*(1), 33–63. https://doi.org/10.1175/JPO-D-14-0045.1

Gladish, C. V., Holland, D. M., Rosing-Asvid, A., Behrens, J. W., & Boje, J. (2014). Oceanic boundary conditions for jakobshavn glacier. Part I: Variability and renewal of ilulissat icefjord waters, 2001–14. *Journal of Physical Oceanography*, *45*(1), 3–32. https://doi.org/10.1175/JPO-D-14-0044.1

Griffies, S. M., & Hallberg, R. W. (2000). Biharmonic friction with a Smagorinsky-like viscosity for use in large-scale Eddy-permitting ocean models. *Monthly Weather Review*, *128*(8), 2935–2946. https://doi.org/10.1175/1520-0493(2000)128⟨2935:BFWASL⟩2.0.CO;2

Hager, A. O., Sutherland, D. A., Amundson, J. M., Jackson, R. H., Kienholz, C., Motyka, R. J., & Nash, J. D. (2022). Subglacial discharge reflux and buoyancy forcing drive seasonality in a silled glacial fjord. *Journal of Geophysical Research: Oceans*, *127*(5). https://doi.org/10.1029/2021JC018355

Harden, B. E., Renfrew, I. A., & Petersen, G. N. (2011). A climatology of wintertime barrier winds off southeast Greenland. *Journal of Climate*, *24*(17), 4701–4717. https://doi.org/10.1175/2011JCLI4113.1

Harden, B. E., Straneo, F., & Sutherland, D. A. (2014). Moored observations of synoptic and seasonal variability in the East Greenland Coastal Current. *Journal of Geophysical Research: Oceans*, *119*(12), 8838–8857. https://doi.org/10.1002/2014JC010134

Hersbach, H., Bell, B., Berrisford, P., Hirahara, S., Horányi, A., Muñoz-Sabater, J., et al. (2020). The ERA5 global reanalysis. *Quarterly Journal of the Royal Meteorological Society*, *146*(730), 1999–2049. https://doi.org/10.1002/qj.3803

Holland, D. M., Thomas, R. H., de Young, B., Ribergaard, M. H., & Lyberth, B. (2008). Acceleration of Jakobshavn Isbræ triggered by warm subsurface ocean waters. *Nature Geoscience*, *1*(10), 659–664. https://doi.org/10.1038/ngeo316

Hopwood, M. J., Carroll, D., Dunse, T., Hodson, A., Holding, J. M., Iriarte, J. L., et al. (2020). Review article: How does glacier discharge affect marine biogeochemistry and primary production in the Arctic? *The Cryosphere*, *14*(4), 1347–1383. https://doi.org/10.5194/tc-14-1347-2020

Howat, I. M., Joughin, I., Tulaczyk, S., & Gogineni, S. (2005). Rapid retreat and acceleration of Helheim Glacier, east Greenland. *Geophysical Research Letters*, *32*(22). https://doi.org/10.1029/2005GL024737

Hughes, K. (2023). Sermilik Fjord, MITgcm simulations, Sanchez et al. [Dataset]. *Zenodo*. https://doi.org/10.5281/zenodo.8356594

Hughes, K. G. (2022). Pathways, form drag, and turbulence in simulations of an ocean flowing through an ice mélange. *Journal of Geophysical Research: Oceans*, *127*(6), e2021JC018228. https://doi.org/10.1029/2021JC018228

Hughes, K. G., Klymak, J. M., Williams, W. J., & Melling, H. (2018). Tidally modulated internal hydraulic flow and energetics in the Central Canadian Arctic Archipelago. *Journal of Geophysical Research: Oceans*, *123*(8), 5210–5229. https://doi.org/10.1029/2018JC013770

Inall, M. E., Nilsen, F., Cottier, F. R., & Daae, R. (2015). Shelf/fjord exchange driven by coastal-trapped waves in the arctic. *Journal of Geophysical Research: Oceans*, *120*(12), 8283–8303. https://doi.org/10.1002/2015JC011277

Jackett, D. R., & Mcdougall, T. J. (1995). Minimal adjustment of hydrographic profiles to achieve static stability. *Journal of Atmospheric and Oceanic Technology*, *12*(2), 381–389. https://doi.org/10.1175/1520-0426(1995)012⟨0381:MAOHPT⟩2.0.CO;2

Jackson, R. H., Lentz, S. J., & Straneo, F. (2018). The dynamics of shelf forcing in Greenlandic fjords. *Journal of Physical Oceanography*, *48*(11), 2799–2827. https://doi.org/10.1175/JPO-D-18-0057.1

Jackson, R. H., Motyka, R. J., Amundson, J. M., Abib, N., Sutherland, D. A., Nash, J. D., & Kienholz, C. (2022). The relationship between submarine melt and subglacial discharge from observations at a tidewater glacier. *Journal of Geophysical Research: Oceans*, *127*(10), e2021JC018204. https://doi.org/10.1029/2021JC018204

Jackson, R. H., Nash, J. D., Kienholz, C., Sutherland, D. A., Amundson, J. M., ka, R. J., et al. (2020). Meltwater intrusions reveal mechanisms for rapid submarine melt at a tidewater glacier. *Geophysical Research Letters*, *47*(2), e2019GL085335. https://doi.org/10.1029/2019GL085335

Jackson, R. H., & Straneo, F. (2016). Heat, salt, and freshwater budgets for a glacial fjord in Greenland. *Journal of Physical Oceanography*, *46*(9), 2735–2768. https://doi.org/10.1175/JPO-D-15-0134.1

Jackson, R. H., Straneo, F., & Sutherland, D. A. (2014). Externally forced fluctuations in ocean temperature at Greenland glaciers in non-summer months. *Nature Geoscience*, *7*, 503–508. https://doi.org/10.1038/ngeo2186

Jenkins, A. (2011). Convection-driven melting near the grounding lines of ice shelves and tidewater glaciers. *Journal of Physical Oceanography*, *41*(12), 2279–2294. https://doi.org/10.1175/JPO-D-11-03.1

Kajanto, K., Straneo, F., & Nisancioglu, K. (2023). Impact of icebergs on the seasonal submarine melt of Sermeq Kujalleq. *The Cryosphere*, *17*(1), 371–390. https://doi.org/10.5194/tc-17-371-2023

Khazendar, A., Fenty, I. G., Carroll, D., Gardner, A., Lee, C. M., Fukumori, I., et al. (2019). Interruption of two decades of Jakobshavn Isbrae acceleration and thinning as regional ocean cools. *Nature Geoscience*, *12*(4), 277–283. https://doi.org/10.1038/s41561-019-0329-3

Kimura, S., Holland, P. R., Jenkins, A., & Piggott, M. (2014). The effect of meltwater plumes on the melting of a vertical glacier face. *Journal of Physical Oceanography*, *44*(12), 3099–3117. https://doi.org/10.1175/JPO-D-13-0219.1

Klinck, J. M., O'Brien, J. J., & Svendsen, H. (1981). A simple model of fjord and coastal circulation interaction. *Journal of Physical Oceanography*, *11*(12), 1612–1626. https://doi.org/10.1175/1520-0485(1981)011⟨1612:ASMOFA⟩2.0.CO;2

Large, W. G., McWilliams, J. C., & Doney, S. C. (1994). Oceanic vertical mixing: A review and a model with a nonlocal boundary layer parameterization. *Review of Geophysics*, *32*(4), 363–403. https://doi.org/10.1029/94RG01872

Lindeman, M. R., Straneo, F., Wilson, N. J., Toole, J. M., Krishfield, R. A., Beaird, N. L., et al. (2020). Ocean circulation and variability beneath Nioghalvfjerdsbræ(79 north glacier) ice tongue. *Journal of Geophysical Research: Oceans*, *125*(8), e2020JC016091. https://doi.org/10.1029/2020JC016091

Liu, Y., MacCready, P., Hickey, B. M., Dever, E. P., Kosro, P. M., & Banas, N. S. (2009). Evaluation of a coastal ocean circulation model for the Columbia River plume in summer 2004. *Journal of Geophysical Research*, *114*(C2). https://doi.org/10.1029/2008JC004929

Lorenz, M., Klingbeil, K., & Burchard, H. (2020). Numerical study of the exchange flow of the Persian Gulf using an extended total exchange flow analysis framework. *Journal of Geophysical Research: Oceans*, *125*(2), e2019JC015527. https://doi.org/10.1029/2019JC015527

Lorenz, M., Klingbeil, K., MacCready, P., & Burchard, H. (2019). Numerical issues of the Total Exchange Flow (TEF) analysis framework for quantifying estuarine circulation. *Ocean Science*, *15*(3), 601–614. https://doi.org/10.5194/os-15-601-2019

Luckman, A., Murray, T., de Lange, R., & Hanna, E. (2006). Rapid and synchronous ice-dynamic changes in East Greenland. *Geophysical Research Letters*, *33*(3). https://doi.org/10.1029/2005GL025428

MacCready, P. (2011). Calculating estuarine exchange flow using isohaline coordinates. *Journal of Physical Oceanography*, *41*(6), 1116–1124. https://doi.org/10.1175/2011JPO4517.1

MacCready, P., & Geyer, W. R. (2010). Advances in estuarine physics. *Annual Review of Marine Science*, *2*(1), 35–58. https://doi.org/10.1146/annurev-marine-120308-081015

MacCready, P., Geyer, W. R., & Burchard, H. (2018). Estuarine exchange flow is related to mixing through the salinity variance budget. *Journal of Physical Oceanography*, *48*(6), 1375–1384. https://doi.org/10.1175/JPO-D-17-0266.1

Mankoff, K. D., Solgaard, A., Colgan, W., Ahlstrøm, A. P., Khan, S. A., & Fausto, R. S. (2020). Greenland Ice Sheet solid ice discharge from 1986 through March 2020. *Earth System Science Data*, *12*(2), 1367–1383. https://doi.org/10.5194/essd-12-1367-2020

Mankoff, K. D., Straneo, F., Cenedese, C., Das, S. B., Richards, C. G., & Singh, H. (2016). Structure and dynamics of a subglacial discharge plume in a Greenlandic fjord. *Journal of Geophysical Research: Oceans*, *121*(12), 8670–8688. https://doi.org/10.1002/2016JC011764

Marshall, J., Adcroft, A., Hill, C., Perelman, L., & Heisey, C. (1997). A finite-volume, incompressible Navier Stokes model for studies of the ocean on parallel computers. *Journal of Geophysical Research*, *102*(C3), 5753–5766. https://doi.org/10.1029/96JC02775

Moffat, C. (2014). Wind-driven modulation of warm water supply to a proglacial fjord. *jorge montt glacier, patagonia*, *41*(11), 3943–3950. https://doi.org/10.1002/2014GL060071

Moon, T., Sutherland, D. A., Carroll, D., Felikson, D., Kehrl, L., & Straneo, F. (2018). Subsurface iceberg melt key to Greenland fjord freshwater budget. *Nature Geoscience*, *11*(1), 49–54. https://doi.org/10.1038/s41561-017-0018-z

Morlighem, M., Williams, C. N., Rignot, E., An, L., Arndt, J. E., Bamber, J. L., et al. (2017). BedMachine v3: Complete bed topography and ocean bathymetry mapping of Greenland from multibeam echo sounding combined with mass conservation. *Geophysical Research Letters*, *44*(21), 11051–11061. https://doi.org/10.1002/2017GL074954

Mortensen, J., Bendtsen, J., Lennert, K., & Rysgaard, S. (2014). Seasonal variability of the circulation system in a west Greenland tidewater outlet glacier fjord, Godthåbsfjord (64°N). *J. Geophys. Res.Earth Surface*, *119*(12), 2591–2603. https://doi.org/10.1002/2014JF003267

Mortensen, J., Lennert, K., Bendtsen, J., & Rysgaard, S. (2011). Heat sources for glacial melt in a sub-arctic fjord (godthåbsfjord) in contact with the Greenland ice sheet. *Journal of Geophysical Research*, *116*(C1), C01013. https://doi.org/10.1029/2010JC006528

Mortensen, J., Rysgaard, S., Arendt, K. E., Juul-Pedersen, T., Søgaard, D. H., Bendtsen, J., & Meire, L. (2018). Local coastal water masses control heat levels in a west Greenland tidewater outlet glacier fjord. *Journal of Geophysical Research: Oceans*, *123*(11), 8068–8083. https://doi.org/10.1029/2018JC014549

Mouginot, J., Rignot, E., Bjørk, A. A., van den Broeke, M., Millan, R., Morlighem, M., et al. (2019). Forty-six years of Greenland Ice Sheet mass balance from 1972 to 2018. *Proceedings of the National Academy of Sciences*, *116*(19), 9239–9244. https://doi.org/10.1073/pnas.1904242116

Muilwijk, M., Straneo, F., Slater, D. A., Smedsrud, L. H., Holte, J., Wood, M., et al. (2022). Export of ice sheet meltwater from Upernavik fjord, west Greenland. *Journal of Physical Oceanography*, *52*(3), 363–382. https://doi.org/10.1175/JPO-D-21-0084.1

Murphy, A. H. (1988). Skill scores based on the mean square error and their relationships to the correlation coefficient. *Monthly Weather Review*, *116*(12), 2417–2424. https://doi.org/10.1175/1520-0493(1988)116⟨2417:SSBOTM⟩2.0.CO;2

Nguyen, A. T., Pillar, H., Ocaña, V., Bigdeli, A., Smith, T. A., & Heimbach, P. (2021). The Arctic Subpolar Gyre sTate Estimate: Description and assessment of a data-constrained, dynamically consistent ocean-sea ice estimate for 2002–2017. *Journal of Advances in Modeling Earth Systems*, *13*(5), e2020MS002398. https://doi.org/10.1029/2020MS002398

Rabinovich, A. B., Shevchenko, G. V., & Thomson, R. E. (2007). Sea ice and current response to the wind: A vector regressional analysis approach. *Journal of Atmospheric and Oceanic Technology*, *24*(6), 1086–1101. https://doi.org/10.1175/JTECH2015.1

Ralston, D. K., Geyer, W. R., & Lerczak, J. A. (2010). Structure, variability, and salt flux in a strongly forced salt wedge estuary. *Journal of Geophysical Research*, *115*(C6). https://doi.org/10.1029/2009JC005806

Rignot, E., Xu, Y., Menemenlis, D., Mouginot, J., Scheuchl, B., Li, X., et al. (2016). Modeling of ocean-induced ice melt rates of five west Greenland glaciers over the past two decades. *Geophysical Research Letters*, *43*(12), 6374–6382. https://doi.org/10.1002/2016GL068784

Rysgaard, S., Vang, T., Stjernholm, M., Rasmussen, B., Windelin, A., & Kiilsholm, S. (2003). Physical conditions, carbon transport, and climate change impacts in a Northeast Greenland fjord. *Arctic Antarctic and Alpine Research*, *35*(3), 301–312. https://doi.org/10.1657/1523-0430(2003)035[0301:PCCTAC]2.0.CO;2

Sanchez, R., Slater, D., & Straneo, F. (2023). Delayed Freshwater Export from a Greenland tidewater glacial fjord. *Journal of Physical Oceanography*, *1*(aop), 1291–1309. https://doi.org/10.1175/JPO-D-22-0137.1

Sanchez, R., Straneo, F., & Andres, M. (2021). Using acoustic travel time to monitor the heat variability of glacial fjords. *Journal of Atmospheric and Oceanic Technology*, *38*(9), 1535–1550. https://doi.org/10.1175/JTECH-D-20-0176.1

Schaffer, J., Kanzow, T., von Appen, W.-J., von Albedyll, L., Arndt, J. E., & Roberts, D. H. (2020). Bathymetry constrains ocean heat supply to Greenland's largest glacier tongue. *Nature Geoscience*, *13*(3), 227–231. https://doi.org/10.1038/s41561-019-0529-x

Schulz, K., Nguyen, A. T., & Pillar, H. R. (2022). An improved and observationally-constrained melt rate parameterization for vertical ice fronts of marine terminating glaciers. *Geophysical Research Letters*, *49*(18), e2022GL100654. https://doi.org/10.1029/2022GL100654

Sciascia, R., Straneo, F., Cenedese, C., & Heimbach, P. (2013). Seasonal variability of submarine melt rate and circulation in an East Greenland fjord. *Journal of Geophysical Research: Oceans*, *118*(5), 2492–2506. https://doi.org/10.1002/jgrc.20142

Shroyer, E. L., Padman, L., Samelson, R. M., Münchow, A., & Stearns, L. A. (2017). Seasonal control of Petermann Gletscher ice-shelf melt by the ocean's response to sea-ice cover in Nares Strait. *Journal of Glaciology*, *63*(238), 324–330. https://doi.org/10.1017/jog.2016.140

Slater, D. A., Carroll, D., Oliver, H., Hopwood, M. J., Straneo, F., Wood, M., et al. (2022). Characteristic depths, fluxes, and timescales for Greenland's tidewater glacier fjords from subglacial discharge-driven upwelling during summer. *Geophysical Research Letters*, *49*(10), e2021GL097081. https://doi.org/10.1029/2021GL097081

Slater, D. A., Felikson, D., Straneo, F., Goelzer, H., Little, C. M., Morlighem, M., et al. (2020). Twenty-first century ocean forcing of the Greenland ice sheet for modelling of sea level contribution. *The Cryosphere*, *14*(3), 985–1008. https://doi.org/10.5194/tc-14-985-2020

Slater, D. A., & Straneo, F. (2022). Submarine melting of glaciers in Greenland amplified by atmospheric warming. *Nature Geoscience*, *15*(10), 1–6. https://doi.org/10.1038/s41561-022-01035-9

Slater, D. A., Straneo, F., Das, S. B., Richards, C. G., Wagner, T. J. W., & Nienow, P. W. (2018). Localized plumes drive front-wide ocean melting of a Greenlandic tidewater glacier. *Geophysical Research Letters*, *45*(22), 12350–12358. https://doi.org/10.1029/2018GL080763

Snow, T., Straneo, F., Holte, J., Grigsby, S., Abdalati, W., & Scambos, T. (2021). More than skin deep: Sea surface temperature as a means of inferring Atlantic water variability on the southeast Greenland continental shelf near Helheim Glacier. *Journal of Geophysical Research: Oceans*, *126*(4), e2020JC016509. https://doi.org/10.1029/2020JC016509

Snow, T., Zhang, W., Schreiber, E., Siegfried, M., Abdalati, W., & Scambos, T. (2023). Alongshore winds force warm Atlantic water toward Helheim Glacier in southeastsoutheast Greenland. *Journal of Geophysical Research: Oceans*, *128*(9), e2023JC019953. https://doi.org/10.1029/2023JC019953

Straneo, F. (2021). Temperature, salinity, dissolved oxygen, and turbidity profiles from sermilik fjord, east Greenland collected over July 7-15, 2017. [Dataset]. *Arctic Data Center*. https://doi.org/10.18739/A2NG4GS8C

Straneo, F. (2024a). Temperature and salinity observations from a mooring outside of Sermilik fjord from august 2013 to august 2016. [Dataset]. *Arctic Data Center*. https://doi.org/10.18739/A21834438

Straneo, F. (2024b). Temperature and salinity observations from a mooring outside of Sermilik fjord from august 2015 to July 2017. [Dataset]. *Arctic Data Center*. https://doi.org/10.18739/A2513TX64

Straneo, F. (2024c). Temperature and salinity observations from a shallow mooring in sermilik fjord from august 2015 to July 2017. [Dataset]. *Arctic Data Center*. https://doi.org/10.18739/A2WH2DG88

Straneo, F. (2024d). Temperature, Salinity, and Velocity observations from a deep mooring in sermilik fjord from august 2015 to July 2017. [Dataset]. *Arctic Data Center*. https://doi.org/10.18739/A2SQ8QK3B

Straneo, F. (2024e). Temperature, salinity, and velocity observations from a mooring outside of sermilik fjord from august 2015 to July 2017. [Dataset]. *Arctic Data Center*. https://doi.org/10.18739/A28P5VB7N

Straneo, F., & Cenedese, C. (2015). The dynamics of Greenland's glacial fjords and their role in climate. *Annual Review of Marine Science*, *7*(1), 89–112. https://doi.org/10.1146/annurev-marine-010213-135133

Straneo, F., Curry, R. G., Sutherland, D. A., Hamilton, G. S., Cenedese, C., Våge, K., & Stearns, L. A. (2011). Impact of fjord dynamics and glacial runoff on the circulation near Helheim Glacier. *Nature Geoscience*, *4*(5), 322–327. https://doi.org/10.1038/ngeo1109

Straneo, F., Hamilton, G. S., Sutherland, D. A., Stearns, L. A., Davidson, F., Hammill, M. O., et al. (2010). Rapid circulation of warm subtropical waters in a major glacial fjord in east Greenland. *Nature Geoscience*, *3*, 182–186. https://doi.org/10.1038/ngeo764

Straneo, F., & Heimbach, P. (2013). North Atlantic warming and the retreat of Greenland's outlet glaciers. *Nature*, *504*(7478), 36–43. https://doi.org/10.1038/nature12854

Straneo, F., & Holte, J. (2018). Water temperature and salinity data from ctd taken from the research vessel adolf jensen collected in the sermilik fjord from 2015-08-02 to 2015-08-11. [Dataset]. *NOAA National Centers for Environmental Information*. Retrieved from http://accession.nodc.noaa.gov/0171277

Straneo, F., Sutherland, D. A., Stearns, L., Catania, G., Heimbach, P., Moon, T., et al. (2019). The case for a sustained Greenland Ice Sheet-Ocean observing system (GrIOOS). *Frontiers in Marine Science*, *6*. https://doi.org/10.3389/fmars.2019.00138

Stuart-Lee, A. E., Mortensen, J., Kaaden, A.-S. v. d., & Meire, L. (2021). Seasonal hydrography of Ameralik: A southwest Greenland fjord impacted by a land-terminating glacier. *Journal of Geophysical Research: Oceans*, *126*(12), e2021JC017552. https://doi.org/10.1029/2021JC017552

Sundfjord, A., Albretsen, J., Kasajima, Y., Skogseth, R., Kohler, J., Nuth, C., et al. (2017). Effects of glacier runoff and wind on surface layer dynamics and Atlantic Water exchange in Kongsfjorden, Svalbard; a model study. Estuarine. *Coastal and Shelf Science*, *187*, 260–272. https://doi.org/10.1016/j.ecss.2017.01.015

Sutherland, D. A., MacCready, P., Banas, N. S., & Smedstad, L. F. (2011). A model study of the salish sea estuarine circulation. *Journal of Physical Oceanography*, *41*(6), 1125–1143. https://doi.org/10.1175/2011JPO4540.1

Sutherland, D. A., Straneo, F., & Pickart, R. S. (2014). Characteristics and dynamics of two major Greenland glacial fjords. *Journal of Geophysical Research: Oceans*, *119*(6), 3767–3791. https://doi.org/10.1002/2013JC009786

Sutherland, D. A., Straneo, F., Stenson, G. B., Davidson, F. J. M., Hammill, M. O., & Rosing-Asvid, A. (2013). Atlantic water variability on the SE Greenland continental shelf and its relationship to SST and bathymetry. *Journal of Geophysical Research: Oceans*, *118*(2), 847–855. https://doi.org/10.1029/2012JC008354

Wood, M., Rignot, E., Fenty, I., An, L., Bjørk, A., van den Broeke, M., et al. (2021). Ocean forcing drives glacier retreat in Greenland. *Science Advances*, *7*(1), eaba7282. https://doi.org/10.1126/sciadv.aba7282

Wood, M., Rignot, E., Fenty, I., Menemenlis, D., Millan, R., Morlighem, M., et al. (2018). Ocean-induced melt triggers glacier retreat in Northwest Greenland. *Geophysical Research Letters*, *45*(16), 8334–8342. https://doi.org/10.1029/2018GL078024

Xu, Y., Rignot, E., Menemenlis, D., & Koppes, M. (2012). Numerical experiments on subaqueous melting of Greenland tidewater glaciers in response to ocean warming and enhanced subglacial discharge. *Annals of Glaciology*, *53*(60), 229–234. https://doi.org/10.3189/2012AoG60A139

Zhao, K. X., Stewart, A. L., & McWilliams, J. C. (2021). Geometric constraints on glacial fjord–shelf exchange. *Journal of Physical Oceanography*, *51*(4), 1223–1246. https://doi.org/10.1175/JPO-D-20-0091.1

Zhao, K. X., Stewart, A. L., & McWilliams, J. C. (2022). Linking overturning, recirculation, and melt in glacial fjords. *Geophysical Research Letters*, *49*(15). https://doi.org/10.1029/2021GL095706

Zhao, K. X., Stewart, A. L., McWilliams, J. C., Fenty, I. G., & Rignot, E. J. (2022). Standing eddies in glacial fjords and their role in fjord circulation and melt. *Journal of Physical Oceanography*, *1*(aop). https://doi.org/10.1175/JPO-D-22-0085.1